IN-SITU NMR STUDY OF MOLECULAR AND IONIC PROCESSES INSIDE CARBON NANOPORES

Zhixiang Luo

A dissertation submitted to the faculty of the University of North Carolina at Chapel Hill in partial fulfillment of the requirements for the degree of Doctor of Philosophy in the Department of Physics and Astronomy.

Chapel Hill
2015

Approved by:

Yue Wu

Laurie E. McNeil

Sean Washburn

Rosa T. Branca

Charles R. Evans

Keith E. Gubbins

Warren S. Warren

ABSTRACT

Zhixiang Luo: *In-situ* NMR Study of Molecular and Ionic Processes inside Carbon Nanopores
(Under the direction of Yue Wu)

Interactions of simple ions with water and interfaces play critical roles in many electrochemical and biological processes. They are especially significant in nanoconfined regions and have a profound impact in many applications, for instance nanofluidics and supercapacitors. This dissertation employs a nuclear magnetic resonance (NMR) technique to study their influence on the ionic processes inside carbon nanopores. To characterize the carbon micropore structure, a convenient NMR method is established by taking a ^{1}H magic angle spinning (MAS) spectrum of the adsorbed water. A density functional theory (DFT) computation of the nucleus-independent chemical shift (NICS) yields a quantitative relationship between the NICS values and the micropore sizes. The carbon micropore size and distribution are derived from the chemical shift and the spectrum lineshape. For aqueous electrolytes inside uncharged carbon nanopores, the measurement of ion concentrations reveals a substantial electroneutrality breakdown. The specific ion effects and ion-ion correlations are shown to play crucial roles in determining the degree of electroneutrality breakdown. The importance of those interactions is further revealed by the asymmetric and nonlinear responses of ion concentrations to the charging of the confining carbon walls. Such information is obtained with a carbon supercapacitor built into the NMR probe. The NMR observations are validated by a numerical calculation of the ion distribution in the nanopores using the generalized Poisson-Boltzmann (PB) equation, demonstrating that the nonelectrostatic interfacial interactions can indeed dominate the electrostatic interactions and lead to the breakdown of electroneutrality inside nanoconfined

regions. Interfacial ion hydration is an essential part of the specific ion effects. Using *in-situ* ^{23}Na and ^{19}F NMR on carbon supercapacitors with different carbon pore sizes, I provide a molecular-scale understanding of the permeation and dehydration of ions in voltage-gated carbon nanopores.

To my beloved grandparents

And my lovely girlfriend Lan

ACKNOWLEDGEMENTS

First and foremost, I would like to express my deepest appreciation to my advisor, Prof. Yue Wu, for his guidance, help and encouragement throughout my PhD study. I have learned so much as a result of his philosophy and action of teaching students in accordance with their aptitude during the past five years, from research details such as the experiment design, data analysis and presentations, to qualities critical for a successful scientist such as curiosity, patience and creativity. His influence on me was far beyond the scientific research.

I am also grateful to Dr. Alfred Kleinhammes who guided me into the magic kingdom of NMR. His training and help made it much easier for me to handle new NMR techniques and to design and modify NMR probes, especially at the beginning of this project.

I would like to thank Prof. Warren Warren in Duke University who allowed me to audit his NMR class in 2013 spring. He showed me the beauty of NMR with broad knowledge and clear explanations. The theories and techniques I learned from his class were extremely helpful for my research.

I would like to express my special gratitude to Dr. Yi-Qiao Song and Dr. Jeffrey Paulsen during the internship at Schlumberger Doll research center. They introduced me to the exciting applications of NMR in the oil industry. The numerical calculation would not have been possible without the Matlab programming skills I gained during the internship.

I am grateful to my committee members, Profs. Yue Wu, Laurie E. McNeil, Sean Washburn, Warren Warren, Keith Gubbins, Charles Evans, and Rosa T. Branca for their advice on the research project and the valuable suggestions on my dissertation.

I have had a lot of help from the previous and current members of Wu's Group. These members are: Gregory Mogilevsky, Haijing Wang, B. J. Anderson, Magdalena Sandor, Courtney Hadsell, Jacob Forstater, Shaun Gidcumb, Yunzhao Xing, Yanchun Ling, Yuan Chong, Patrick Doyle and Yan Song. In particular, the discussions with Yunzhao Xing were very insightful and fruitful. He also helped me with the DFT calculation.

Last but not least, I want to take this opportunity to thank my family. I couldn't have achieved this without their selfless support, financially and spiritually. My girlfriend Lan from NC State University shares all my happiness and sorrows since 2012. She is always with me during my low times, no matter it being research difficulty or family loss. Her acceptance is the best cure that cheers me up. My grandparents and parents have sacrificed a lot to raise me and support my higher education. Their love is priceless.

TABLE OF CONTENTS

LIST OF TABLES

LIST OF FIGURES

LIST OF ABBREVIATIONS

AC	Activated Carbon
BET	Brunauer-Emmett-Teller
BO	Burn-Off
DFT	Density Functional Theory
EDL	Electric Double Layer
EDLC	Electric Double Layer Capacitor
FWHM	Full-Width at Half-Maximum
GIAO	Gauge-Independent Atomic Orbital
MAS	Magic Angle Spinning
NICS	Nucleus-Independent Chemical Shift
NMR	Nuclear Magnetic Resonance
PEEK	Poly (Ether Ether Ketone)
PB	Poisson-Boltzmann
PSD	Pore Size Distribution
RTIL	Room Temperature Ionic Liquid
SAM	Self-Assembled Monolayer
SEM	Scanning Electron Microscope
SHG	Second Harmonic Generation Spectroscopy
SSA	Specific Surface Area
TEM	Transmission Electron Microscope
TMS	Tetramethylsilane
VSFG	Vibrational Sum Frequency Generation Spectroscopy

CHAPTER 1 INTRODUCTION

1.1 Motivation

1.1.1 Specific Ion Effects and the Hofmeister Series

Ions are hydrated in aqueous electrolytes; the hydration structure and dynamics can be quite complex with interactions such as the dispersion forces and the hydrogen bonding playing important roles [1-13]. The properties of ion hydration vary significantly from ion to ion, even amongst ions with the same electrovalency (e.g. F^- and I^-), thus they are ion-specific in contrast to the Coulomb interactions. When the ions in solutions are presented with an interface, unexpected phenomena can emerge because of the interplay between the ion, the solvent water and the surface via Coulombic and ion-specific nonelectrostatic interactions. Strongly hydrated ions such as F^- and Na^+ may prefer the bulk aqueous environment instead of the interface between water and a hydrophobic surface; in contrast, weakly hydrated ions may prefer the interface [14-18], as demonstrated in Figure 1.1.

Ions vary in their effects on other fundamental properties of ionic solutions. Such specific ion effects have both fascinated and challenged the scientific community over more than a century, dating back to the report by Franz Hofmeister about ionic properties, arranged in series, with respect to their relative influence on the precipitation of egg white proteins from aqueous solutions [19-22]. This series, named the Hofmeister series, was found later to apply to a whole range of phenomena including viscosity, surface tension, freezing point depression and water activity coefficient etc. [17,18,23,24], with only minor changes of the order depending on the property investigated.

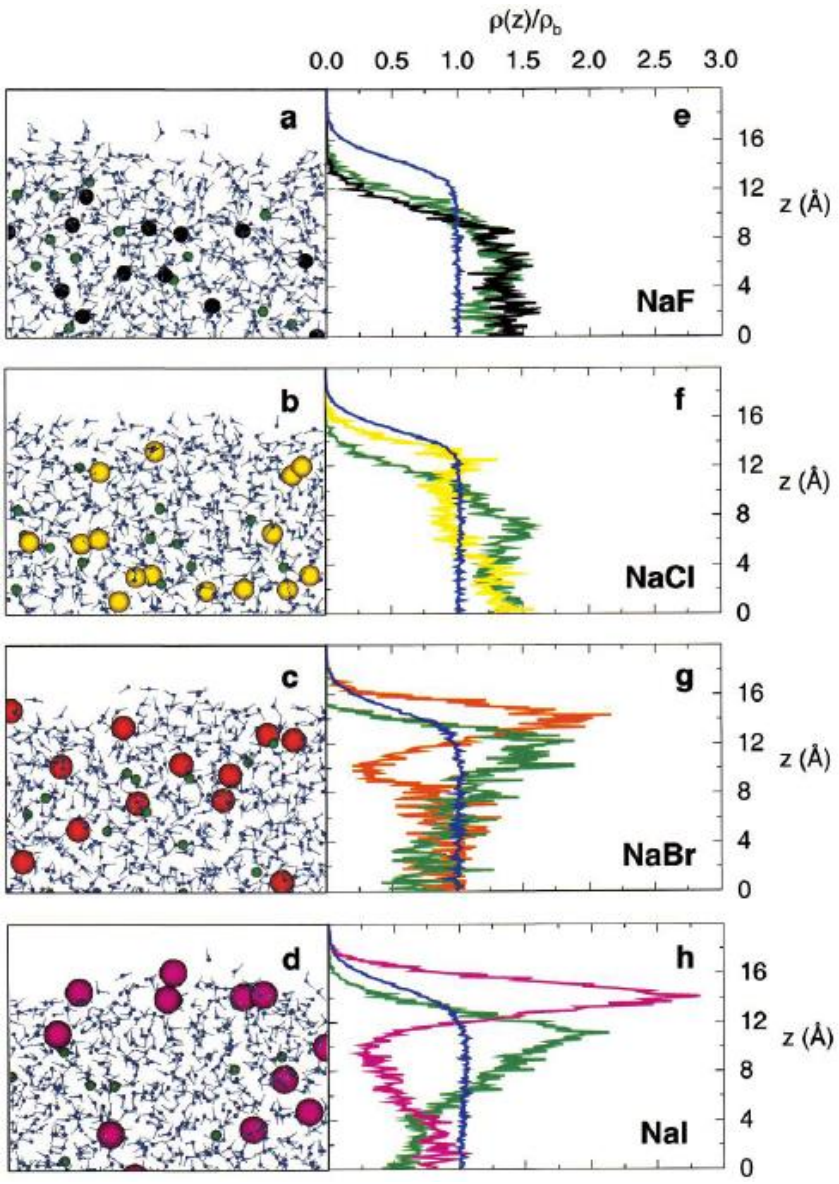

Figure 1.1: The specific ion effects on the ion distribution near the solution/air interface. (a-d): Snapshots of the molecular dynamics simulations. The coloring scheme is: water oxygen, blue; water hydrogen, gray; sodium ions, green; chloride ions, yellow; bromide ions, orange; iodide ions, magenta. (e-h): Densities (normalized by the bulk density) of water oxygen atoms and ions plotted vs. the z-distance in the direction normal to the interface. The colors of the curves correspond to the colors of the atoms in the snapshots. [25]

Below is the generally accepted ranking for anions although minor differences exist in different studies [17,18]:

$$CO_3^{2-} \quad SO_4^{2-} \quad S_2O_3^{2-} \quad H_2PO_4^- \quad F^- \quad Cl^- \quad Br^- \quad NO_3^- \quad I^- \quad ClO_4^- \quad SCN^-$$

The anions to the left side of Cl^- are called kosmotropes (structure-makers), which promote the salting-out of proteins, increase the surface tension of aqueous solution, and induce a wide range of other effects. In contrast, the anions to the right side of Cl^- are called chaotropes (structure-breakers), which promote the salting-in of proteins, decrease the surface tension of aqueous solution, and also induce a wide range of other effects. The ranking for cations is much less systematic and is based on the salting-out efficiency. Some cations of interests are ranked below [18,26]:

$$Li^+ \quad Na^+ \quad K^+ \quad Al^{3+} \quad NH_4^+ \quad H^+$$

Although the Hofmeister series is a fundamental framework to study many kinds of biochemical systems involving salty solutions, the underlying mechanism of its general applicability remained unclear for a long time. In the last two decades, the Hofmeister effect has received unprecedented attention. A large amount of experimental and theoretical work was done to study the specific ion effects at the interface [14-16,27-50], leading to exciting discoveries such as the surface enhancement of halides [14-16,29,35,51-54] and insights into the Hofmeister series which reflects the systematic variations in the specific ion effects [17,18,20,24,26,46,55-59]. Experiments indicate that the ion has negligible effects on the water structure beyond the first hydration shell [60], disproving the long-held speculation that the Hofmeister effect is due to the relative ability of ions to change the water structure network (water structure maker/breaker). Instead, the direct ion interactions with the surface play an important and perhaps a dominant role in the interfacial specific ion effects [16-18,23,24,61-65].

Another important area, less explored by experiments, is the consequences of the specific ion effects in the nanoconfined space. Although the theoretical investigations of nanoconfined electrolytes are extremely active [66-71], experimental reports remain scarce [72-81]. The prevalent surface-selective techniques for the study of the specific ion effects, such as the vibrational sum frequency generation spectroscopy (VSFG), the second harmonic generation spectroscopy (SHG) and the X-ray photoelectron spectroscopy, are not applicable for nanoconfined electrolytes.

1.1.2 Nanoconfined Electrolytes

Nanoconfined fluids, especially nanoconfined water, are ubiquitous in nature and often exhibit intriguing properties [72,82-86]. An important special subject of nanoconfined fluids is that of ionic solutions. In particular, aqueous ionic solution is a subject of vital importance but also a subject with major open questions [3-5,7-10,12,60,87-91]. Nanoconfined fluids are relevant to many scientific disciplines ranging from the energy storage in supercapacitors and fuel cells [92-112], to water desalination [113-115], to proteins and ion channels [116,117], and to nanofluidics [118-120].

How ions distribute and migrate inside the nanoconfined space is one of the central and basic scientific questions in nanoconfined electrolytes. In the nanoconfined environment, the influence of the solvent-mediated interfacial effects is amplified due to the relatively small fraction of the bulk phase. As such, unusual phenomena could emerge in nanoconfined ionic solutions, with different ions of the same valence exhibiting very different properties [121,122]. The complexity and subtlety of the ionic processes in the nanoconfinement are reflected by the fact that despite the Nobel Prize winning work on the structure of K^+ ion channel over a decade ago, the detailed mechanism of ion selectivity is still hotly debated [123,124].

The importance of nanoconfined fluids is also exemplified in technological applications such as carbon supercapacitors. A major puzzle in the last decade is the anomalous capacitance increase in pores less than 1 nm [99], shown in Figure 1.2. An explanation could not be achieved without looking at the ion distribution inside the nanopores. However, theoretical and experimental developments in this area are far from sufficient. Supercapacitors store energy in the electric double layer (EDL) formed at the interface between the solid electrode and the liquid electrolyte. But the EDL theory based only on electrostatic considerations, such as the Gouy-Chapman theory, is not applicable in the scenarios of high electrolyte concentration and high electrode voltage.

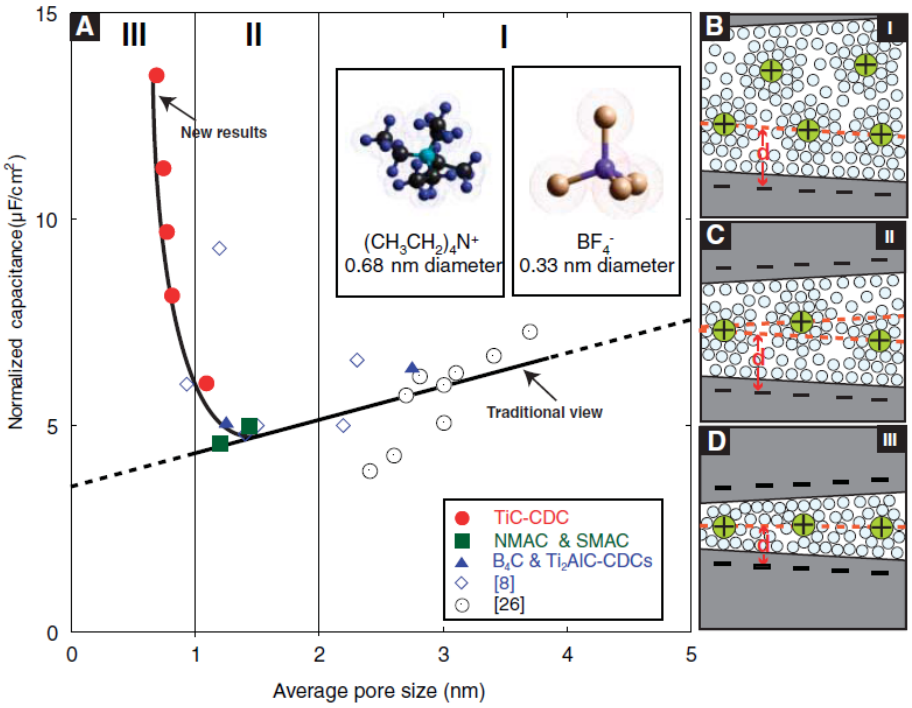

Figure 1.2: The dependence of specific capacitance on the pore size of carbon materials. The capacitance increases sharply when the pore size is less than 1 nm. A quantitative explanation cannot be achieved without looking at the ion distributions which are strongly affected by the specific ion effects in nanoconfinement. [99]

The Gouy-Chapman theory solves the PB equation with simplified assumptions where ions are treated as point charges interacting with their mean field and the solvent is treated as a structureless continuum. The molecular-scale structures, nonelectrostatic ion-surface interactions and ion-ion correlations are ignored. The Gouy-Chapman theory predicts a uniform ion distribution near an uncharged surface, which contradicts with the MD simulation shown in Figure 1.1. Modified theories accounting for the finite ion size [67,125,126], dispersive force [52,53,125,127-129], and ion-ion correlations [52,53,125,127-129] are just emerging, but their application in the nanopore confinement has not been verified by experiments. Moreover, nearly all theoretical simulations of nanoconfined electrolytes have used the charge neutrality condition as a starting point when the confining walls are not charged. This is intuitively expected since a substantial charge imbalance could be energetically unfavorable due to the strong electrostatic repulsion, especially inside a nanoconfined region. However, such an assumption is questionable. As we can see in Figure 1.1, cations and anions are separated near the interface. Inside the very small nanoconfined space, how would the tendency of charge separation induced by the interfacial specific ion effects negotiate with the electroneutrality condition? Can the charge neutrality be violated inside the nanoconfined space? What other unusual consequences can the specific ion effects lead to?

1.1.3 NMR Approach for Nanoconfined Electrolytes and Specific Ion Effects

The objective of this dissertation is to employ the NMR technique to investigate nanoconfined electrolytes. The nanoconfinement is provided by a high quality activated carbon derived from the polymer poly(etheretherketone) (PEEK) [130-133]. Compared to other activated carbons made from natural product precursors, the PEEK-derived carbon has several advantages. Firstly, it has a low density of defects and functional groups. Secondly, the pore size

is able to be tuned from 0.5 nm to 2 nm by controlling the physical activation condition. Thirdly, it consists of mainly micropores (less than 2 nm) and has a very narrow pore size distribution (PSD). All these properties are critical to investigate the manifestation of the specific ion effects in nanoconfined electrolytes and their pore size dependence.

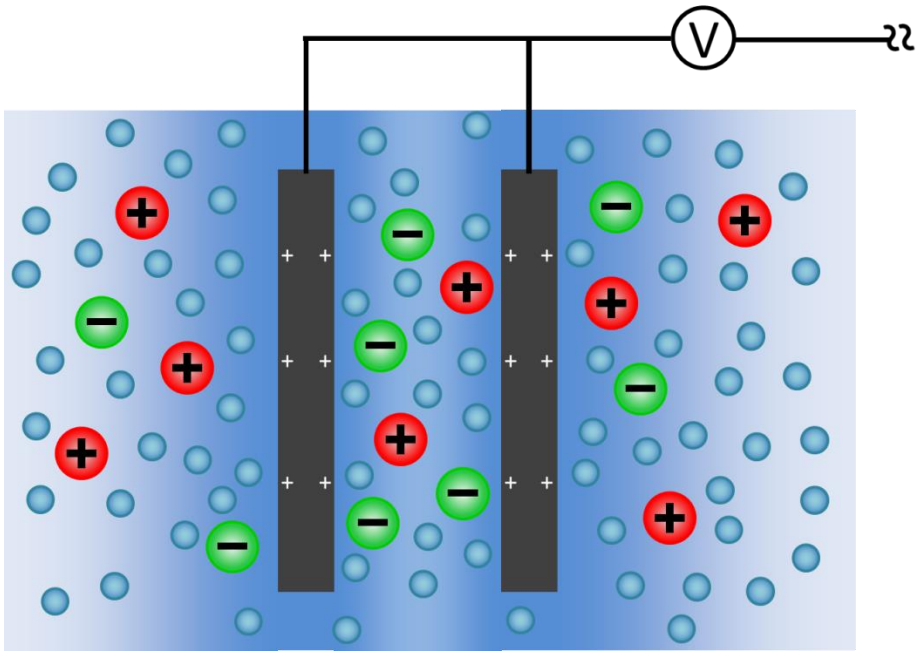

Figure 1.3: Illustration of an electrochemical system consisting of nanoconfined electrolytes in equilibrium with a bulk phase. The PEEK-derived activated carbon provides the confinement and its surface charge can be tuned by applying voltage. Electrolyte properties such as the ion distribution are important for many applications but are very challenging for experimental investigations.

NMR is a quantitative, ion-selective and non-invasive technique well suited for investigating fluids in porous materials, especially in activated carbons [77,134-136]. Previous NMR studies have investigated hydrogen storage [133], electrolyte organization [136], and water adsorption [137] in activated carbons. The uniqueness of the activated carbon system is that the electrolyte confined in the nanopores has a different chemical shift from the electrolyte outside [133,138,139]. As a result, we have a fingerprint to selectively study nanoconfined electrolytes

in equilibrium with a bulk phase, as illustrated in Figure 1.3. Many insights on the ion distribution and transport can be gained by quantifying the average ion concentration in the nanopores.

The role played by the specific ion effects can be evaluated in two ways. One is to systematically explore a series of electrolytes where the anions are chosen from the Hofmeister series and are known to vary in their interfacial interactions. The other way is to tune the surface charge on the confining walls, as shown in Figure 1.3. The contributions from the electrostatic and nonelectrostatic interactions can then be separated. Owing to the good conductivity of activated carbon, the surface charging can be easily achieved by applying a voltage on the carbon electrodes as it is usually done in a carbon supercapacitor.

1.1.4 Dissertation Outline

Chapter 2 describes the synthesis and characterization of the PEEK-derived activated carbon. A series of activated carbon with different pore sizes and narrow PSDs is obtained. A convenient NMR method based on the NICS mechanism is established to characterize the PSD of the activated carbons, with the aid of DFT calculations to establish the quantitative relationship between the NICS value and the pore size.

Chapter 3 reports the NMR measurement of the average ion concentrations inside the carbon nanopores for a series of sodium salts whose anions are chosen from the Hofmeister series. The specific ion effects on the electroneutrality breakdown are evaluated. The dependence of the ion concentrations on the surface charging is measured by the *in-situ* NMR on a carbon supercapacitor. The role of ion-electrostatic ion-surface interactions and ion-ion correlations are discussed.

Chapter 4 focuses on the numerical calculation of the ion distributions inside the nanopores to elucidate the mechanism of the electroneutrality breakdown. The generalized PB equation accounting for the ion-specific interfacial interactions is solved both inside and outside the nanopores simultaneously. A new boundary condition permitting induced surface charge is employed.

Chapter 5 reports the *in-situ* NMR observation of the ion permeation and dehydration in the voltage-gated carbon nanopores. A molecular-scale understanding is provided for the ion transport into nanopores whose size is comparable to the hydrated ion size, shedding lights on the physics of the interfacial specific ion effects in nanoconfinement.

1.2 NMR Principles

NMR is the main technique used in this dissertation to probe the molecular and ionic processes inside activated carbon nanopores. A brief review of the NMR principles is provided here before discussing the *in-situ* NMR results.

1.2.1 Magnetization

A nucleus with spin quantum number I has an angular momentum $I\hbar$ and magnetic moment $\mu = \gamma I\hbar$, where $\hbar$ is the Planck constant and γ is the gyromagnetic ratio. Table 1.1 lists the gyromagnetic ratios for nuclei relevant to this dissertation. When a nucleus is placed in an external static magnetic field B_0 along the z-direction, the interaction energy splits into $2I+1$ levels $E_m = -\vec{\mu} \cdot \vec{B}_0 = -m\gamma\hbar B_0$ with the magnetic quantum number $m = -I, -I+1, \ldots I-1, I$. In thermal equilibrium, the probability for the spin to stay on each energy level follows the Boltzmann distribution, $P_m \propto \exp(-\frac{E_m}{k_B T}) = \exp(\frac{m\gamma\hbar B_0}{k_B T})$. The net magnetization of N non-interacting spins is [140,141]

$$M_0 = N\gamma\hbar \frac{\sum_{m=-I}^{I} m \exp(\frac{m\gamma\hbar B_0}{k_B T})}{\sum_{m=-I}^{I} \exp(\frac{m\gamma\hbar B_0}{k_B T})} \tag{1.1}$$

In the high temperature approximation, i.e. $\gamma\hbar B_0 \ll k_B T$, this reduces to

$$M_0 = \frac{N\gamma^2\hbar^2 B_0 I(I+1)}{3k_B T} \tag{1.2}$$

Table 1.1: Nucleus gyromagnetic ratio and natural abundance [142]

Nucleus	Spin	Natural Abundance (%)	γ $\left(10^6 \text{ rad}\cdot\text{s}^{-1}\cdot\text{T}^{-1}\right)$	$\frac{\gamma}{2\pi}\left(\text{MHz}\cdot\text{T}^{-1}\right)$
^{1}H	1/2	~100	267.522	42.577
^{2}H	1	0.015	41.066	6.536
^{11}B	3/2	80.1	85.847	13.663
^{13}C	1/2	1.1	67.283	10.708
^{15}N	1/2	0.37	-27.126	-4.317
^{19}F	1/2	~100	251.815	40.078
^{23}Na	3/2	~100	70.808	11.269

The nuclear spin precesses along the external magnetic field and is governed by the Hamiltonian

$$H = -\gamma B_0 I_z \tag{1.3}$$

The precession angular frequency, known as the Larmor frequency, is $\omega = -\gamma B_0$. Here the positive and negative signs of γ mean different precession directions.

If an oscillating magnetic field at the Larmor frequency is applied perpendicular to the static field, say $\overrightarrow{B_1} = B_1 \cos(\omega t)\mathbf{x}$, the macroscopic net magnetization is then tipped away from

the z-direction. After the perturbation, the macroscopic net magnetization precesses along the static field B_0 and generates an oscillating electromagnetic signal that can be picked up by a sensitive radio-frequency detector. This signal is often referred to as the free induction decay (FID).

1.2.2 Relaxation

Two relaxation processes are important in the NMR: the transverse relaxation and the longitudinal relaxation. In the classical picture, the Bloch equations describe the time evolution of the net magnetization:

$$\begin{aligned}\frac{dM_x}{dt} &= \gamma(\mathbf{M}\times\mathbf{B})_x - \frac{M_x}{T_2}\\ \frac{dM_y}{dt} &= \gamma(\mathbf{M}\times\mathbf{B})_y - \frac{M_y}{T_2}\\ \frac{dM_z}{dt} &= \gamma(\mathbf{M}\times\mathbf{B})_z - \frac{M_z - M_0}{T_1}\end{aligned} \tag{1.4}$$

where T_2 is the transverse relaxation time and T_1 is the longitudinal relaxation time. After the perturbation which moves the net magnetization from z direction to –y direction, the evolution of the macroscopic magnetization has the form:

$$\begin{aligned}M_x &= M_0 \sin(\omega t)\exp(-t/T_2)\\ M_y &= -M_0 \cos(\omega t)\exp(-t/T_2)\\ M_z &= M_0 - M_0 \exp(-t/T_1)\end{aligned} \tag{1.5}$$

For spin >1/2 nuclei such as ^{23}Na, the electric quadrupole coupling plays a dominant role. For spin 1/2 systems, the most important relaxation mechanism is the through-space dipolar coupling between spins. The rotational and translational motion of the molecule results in a fluctuating magnetic field at the site of spins. For molecules containing only two spins of the

same type, such as ^{1}H in H_2O, the intramolecular dipole-dipole interaction dominates the relaxation process, and the relaxation times are given by [142]

$$\begin{aligned}\frac{1}{T_1} &= \frac{3}{10}b^2[J(\omega)+4J(2\omega)] \\ \frac{1}{T_2} &= \frac{3}{20}b^2[3J(0)+5J(\omega)+2J(2\omega)]\end{aligned} \tag{1.6}$$

where $b = -\frac{\mu_0}{4\pi}\frac{\hbar\gamma^2}{r^3}$ is the dipole-dipole coupling constant (r is the intramolecular distance between the two spins) and $J(\omega) = \frac{\tau_c}{1+\omega^2\tau_c^2}$ is the spectral density, i.e. the Fourier transform of the autocorrelation function (τ_c is the correlation time).

1.2.3 Chemical Shift

The local magnetic field that a spin sees is not exactly the same for all spins even when the external magnetic field $\overrightarrow{B_0}$ is very uniform. It depends on the local electronic environment because electrons are magnetic. This results in changes in the Larmor frequency. The frequency shift depends on the magnetic field strength, but the ratio of the shift over the Larmor frequency is fixed, and this is called the chemical shift in diamagnetic materials, the Knight shift in metals, and the paramagnetic shift in paramagnetic materials. The expression for the chemical shift is as follows:

$$\delta = \frac{\omega - \omega_0}{\omega_0} \tag{1.7}$$

where ω_0 is the Larmor frequency of a reference compound. Tetramethylsilane (TMS) is usually used as the reference for ^{1}H, ^{13}C and ^{29}Si.

The chemical shift is very useful in probing the local structure and environment. In this dissertation, the chemical shift in two scenarios is of particular interest. One is the chemical shift

of hydrated ions which reveals important information on the hydration number. The other is the chemical shift in the activated carbon nanopores. The sensitive dependence of the chemical shift on the nanopore size provides a unique way to measure the PSD [139].

1.3 REFERENCES

1. Thompson, W. H. *Annual Review of Physical Chemistry* **62**, 599-619 (2011).
2. Soniat, M. and Rick, S. W. *J. Chem. Phys.* **137**, 044511-044519 (2012).
3. Kropman, M. F. and Bakker, H. J. *Science* **291**, 2118-2120 (2001).
4. Hinton, J. F. and Amis, E. S. *Chem. Rev.* **71**, 627-674 (1971).
5. Christian, K. and Luigi Delle, S. *J. Phys.: Condens. Matter* **19**, 192101 (2007).
6. Young, R. M. and Neumark, D. M. *Chemical Reviews* **112**, 5553-5577 (2012).
7. Tielrooij, K. J., Garcia-Araez, N., *et al. Science* **328**, 1006-1009 (2010).
8. Laage, D. and Hynes, J. T. *Proc. Natl. Acad. Sci. U.S.A.* **104**, 11167-11172 (2007).
9. Barnett, R. N. and Landman, U. *Phys. Rev. Lett.* **70**, 1775-1778 (1993).
10. Craig, J. D. C. and Brooker, M. H. *J. Solution Chem.* **29**, 879-888 (2000).
11. Mancinelli, R., Botti, A., *et al. Journal of Physical Chemistry B* **111**, 13570-13577 (2007).
12. Marcus, Y. *Chem. Rev.* **109**, 1346-1370 (2009).
13. Mucha, M., Frigato, T., *et al. Journal of Physical Chemistry B* **109**, 7617-7623 (2005).
14. Jungwirth, P. and Tobias, D. J. *Journal of Physical Chemistry B* **105**, 10468-10472 (2001).
15. Jungwirth, P. and Tobias, D. J. *Journal of Physical Chemistry B* **106**, 6361-6373 (2002).
16. Jungwirth, P. and Tobias, D. J. *Chemical Reviews* **106**, 1259-1281 (2006).
17. Zhang, Y. J. and Cremer, P. S. *Curr. Opin. Chem. Biol.* **10**, 658-663 (2006).
18. Lo Nostro, P. and Ninham, B. W. *Chemical Reviews* **112**, 2286-2322 (2012).
19. Parsegian, V. A. *Nature* **378**, 335-336 (1995).
20. Collins, K. D. and Washabaugh, M. W. *Quarterly Reviews of Biophysics* **18**, 323-422 (1985).
21. Wilson, E. K. *Chemical & Engineering News Archive* **85**, 47-49 (2007).

22. Kunz, W., Henle, J., *et al. Current Opinion in Colloid & Interface Science* **9**, 19-37 (2004).

23. Kunz, W., *Specific ion effects*. (World Scientific, Singapore, 2010).

24. Kunz, W., Lo Nostro, P., *et al. Current Opinion in Colloid & Interface Science* **9**, 1-18 (2004).

25. Jungwirth, P. and Tobias, D. J. *J. Phys. Chem. B* **105**, 10468-10472 (2001).

26. Lopez-Leon, T., Santander-Ortega, M. J., *et al. Journal of Physical Chemistry C* **112**, 16060-16069 (2008).

27. Luo, G. M., Malkova, S., *et al. Science* **311**, 216-218 (2006).

28. Laanait, N., Mihaylov, M., *et al. Proceedings of the National Academy of Sciences* **109**, 20326-20331 (2012).

29. Ghosal, S., Hemminger, J. C., *et al. Science* **307**, 563-566 (2005).

30. Cheng, M. H., Callahan, K. M., *et al. Journal of Physical Chemistry C* **116**, 4545-4555 (2012).

31. Xantheas, S. S. and Voth, G. A. *Journal of Physical Chemistry B* **113**, 3997-3999 (2009).

32. Wick, C. D. *Journal of Physical Chemistry A* **117**, 12459-12467 (2013).

33. Vu, T. H. and Shultz, M. J. *Chemical Physics Letters* **572**, 13-15 (2013).

34. Sloutskin, E., Baumert, J., *et al. J. Chem. Phys.* **126** (2007).

35. Levin, Y. and dos Santos, A. P. *Journal of Physics-Condensed Matter* **26** (2014).

36. Kumar, R., Knight, C., *et al. Faraday Discussions* **167**, 263-278 (2013).

37. Jorn, R., Kumar, R., *et al. Journal of Physical Chemistry C* **117**, 3747-3761 (2013).

38. dos Santos, A. P. and Levin, Y. *Faraday Discussions* **160**, 75-87 (2013).

39. dos Santos, A. P. and Levin, Y. *Langmuir* **28**, 1304-1308 (2012).

40. Cummings, O. T. and Wick, C. D. *Journal of Chemical Physics* **139** (2013).

41. Shamay, E. S. and Richmond, G. L. *Journal of Physical Chemistry C* **114**, 12590-12597 (2010).

42. Robertson, E. J., Carpenter, A. P., *et al. Journal of Physical Chemistry C* **118**, 15260-15273 (2014).

43. Robertson, E. J., Beaman, D. K., *et al. Langmuir* **29**, 15511-15520 (2013).

44. Record, M. T., Guinn, E., *et al. Faraday Discussions* **160**, 9-44 (2013).

45. Pegram, L. M. and Record, M. T. *Journal of Physical Chemistry B* **111**, 5411-5417 (2007).

46. Otten, D. E., Shaffer, P. R., *et al. Proceedings of the National Academy of Sciences* **109**, 701-705 (2012).

47. Newberg, J. T., McIntire, T. M., *et al. Journal of Physical Chemistry A* **114**, 9480-9485 (2010).

48. Kelly, D. N., Lam, R. K., *et al. Journal of Physical Chemistry C* **117**, 12702-12706 (2013).

49. Gopalakrishnan, S., Liu, D. F., *et al. Chemical Reviews* **106**, 1155-1175 (2006).

50. Ghosal, S., Brown, M. A., *et al. Journal of Physical Chemistry A* **112**, 12378-12384 (2008).

51. Knipping, E. M., Lakin, M. J., *et al. Science* **288**, 301-306 (2000).

52. Levin, Y., dos Santos, A. P., *et al. Phys. Rev. Lett.* **103**, 257802 (2009).

53. Horinek, D. and Netz, R. R. *Phys. Rev. Lett.* **99**, 226104 (2007).

54. Cheng, J., Vecitis, C. D., *et al. Journal of Physical Chemistry B* **110**, 25598-25602 (2006).

55. Schwierz, N., Horinek, D., *et al. Langmuir* **29**, 2602-2614 (2013).

56. Parsegian, V. A. *Nature* **378**, 335-336 (1995).

57. Gurau, M. C., Lim, S.-M., *et al. J. Am. Chem. Soc.* **126**, 10522-10523 (2004).

58. Lund, M. and Jungwirth, P. *J. Phys.: Condens. Matter* **20**, 494218 (2008).

59. Wilson, E. K. *Chemical & Engineering News* **85**, 47-49 (2007).

60. Omta, A. W., Kropman, M. F., *et al. Science* **301**, 347-349 (2003).

61. Collins, K. D. and Washabaugh, M. W. *Q. Rev. Biophys.* **18**, 323-422 (1985).

62. Zhang, Y. and Cremer, P. S. *Curr. Opin. Chem. Biol.* **10**, 658-663 (2006).

63. Kunz, W. *Current Opinion in Colloid & Interface Science* **15**, 34-39 (2010).

64. Chen, X., Yang, T., *et al. J. Am. Chem. Soc.* **129**, 12272-12279 (2007).

65. Tobias, D. J. and Hemminger, J. C. *Science* **319**, 1197-1198 (2008).

66. Kalcher, I., Schulz, J. C., *et al. J. Chem. Phys.* **133**, 164511 (2010).

67. Kalcher, I., Schulz, J. C., *et al. Phys. Rev. Lett.* **104**, 097802 (2010).

68. Lima, E., Horinek, D., *et al. J. Phys. Chem. B* **112**, 1580-1585 (2008).

69. Bou-Malham, I. and Bureau, L. *Soft Matter* **6**, 4062-4065 (2010).

70. Kalluri, R. K., Konatham, D., *et al. Journal of Physical Chemistry C* **115**, 13786-13795 (2011).

71. Argyris, D., Cole, D. R., *et al. ACS Nano* **4**, 2035-2042 (2010).

72. Ohba, T., Hata, K., *et al. J. Am. Chem. Soc.* **134**, 17850-17853 (2012).

73. Tan, H.-S., Piletic, I. R., *et al. Phys. Rev. Lett.* **94**, 057405 (2005).

74. Moilanen, D. E., Levinger, N. E., *et al. Journal of the American Chemical Society* **129**, 14311-14318 (2007).

75. Fayer, M. D. and Levinger, N. E. *Annual Review of Analytical Chemistry* **3**, 89-107 (2010).

76. Park, S., Moilanen, D. E., *et al. Journal of Physical Chemistry B* **112**, 5279-5290 (2008).

77. Wang, H., Forse, A. C., *et al. J. Am. Chem. Soc.* **135**, 18968-18980 (2013).

78. Forse, A. C., Griffin, J. M., *et al. Physical Chemistry Chemical Physics* **15**, 7722-7730 (2013).

79. Wang, H., Koster, T. K. J., *et al. Journal of the American Chemical Society* **133**, 19270-19273 (2011).

80. Deschamps, M., Gilbert, E., *et al. Nature Materials* **12**, 351-358 (2013).

81. Levi, M. D., Salitra, G., *et al. Nature Materials* **8**, 872-875 (2009).

82. Wang, H. J., Xi, X. K., *et al. Science* **322**, 80-83 (2008).

83. Cazade, P.-A., Hartkamp, R., *et al. J. Phys. Chem. C* **118**, 5061-5072 (2014).

84. Algara-Siller, G., Lehtinen, O., *et al. Nature* **519**, 443-445 (2015).

85. Holt, J. K., Park, H. G., *et al. Science* **312**, 1034-1037 (2006).

86. Baugh, J., Kleinhammes, A., *et al. Science* **294**, 1505-1507 (2001).

87. Afanasiev, V. N., Ustinov, A. N., *et al. J. Phys. Chem. B* **113**, 212-223 (2008).

88. Mancinelli, R., Botti, A., *et al. J. Phys. Chem. B* **111**, 13570-13577 (2007).

89. Headrick, J. M., Diken, E. G., *et al. Science* **308**, 1765-1769 (2005).

90. Raviv, U. and Klein, J. *Science* **297**, 1540-1543 (2002).

91. Marx, D., Chandra, A., *et al. Chem. Rev.* **110**, 2174-2216 (2010).

92. Sharma, T., Mohana Reddy, A. L., *et al. Int. J. Hydrogen Energy* **33**, 6749-6754 (2008).

93. Izadi-Najafabadi, A., Yamada, T., *et al. ACS Nano* **5**, 811-819 (2011).

94. Ling, L. C., Sun, G. W., *et al. Acta Physico-Chimica Sinica* **27**, 449-454 (2011).

95. Daffos, B., Taberna, P. L., *et al. Fuel Cells* **10**, 819-824 (2010).

96. Inagaki, M., Konno, H., *et al. J. Power Sources* **195**, 7880-7903 (2010).

97. Zheng, C., Qi, L., *et al. J. Power Sources* **195**, 4406-4409 (2010).

98. Simon, P. and Gogotsi, Y. *Nat Mater* **7**, 845-854 (2008).

99. Chmiola, J., Yushin, G., *et al. Science* **313**, 1760-1763 (2006).

100. Zhu, Y., Murali, S., *et al. Science* **332**, 1537-1541 (2011).

101. Litster, S., Sinton, D., *et al. J. Power Sources* **154**, 95-105 (2006).

102. Kjeang, E., McKechnie, J., *et al. J. Power Sources* **168**, 379-390 (2007).

103. Chmiola, J., Largeot, C., *et al. Angewandte Chemie* **120**, 3440-3443 (2008).

104. Balducci, A., Dugas, R., *et al. J. Power Sources* **165**, 922-927 (2007).

105. Mucha, M., Frigato, T., *et al. J. Phys. Chem. B* **109**, 7617-7623 (2005).

106. Kastening, B., Hahn, M., *et al. Electrochimica Acta* **42**, 2789-2799 (1997).

107. Barbieri, O., Hahn, M., *et al. Carbon* **43**, 1303-1310 (2005).

108. Vatamanu, J., Borodin, O., *et al. J. Phys. Chem. B* **115**, 3073-3084 (2011).

109. Oren, Y. and Soffer, A. *Journal of Electroanalytical Chemistry and Interfacial Electrochemistry* **186**, 63-77 (1985).

110. Parsons, R. *Chem. Rev.* **90**, 813-826 (1990).

111. Simon, P. and Gogotsi, Y. *Philosophical Transactions of the Royal Society a-Mathematical Physical and Engineering Sciences* **368**, 3457-3467 (2010).

112. Stojek, Z., in *Electroanalytical Methods*, edited by F. Scholz (Springer Berlin Heidelberg, 2010), pp. 3-9.

113. Cohen-Tanugi, D. and Grossman, J. C. *Nano Lett.* **12**, 3602-3608 (2012).

114. Elimelech, M. and Phillip, W. A. *Science* **333**, 712-717 (2011).

115. Oren, Y. *Desalination* **228**, 10-29 (2008).

116. Zhou, Y. F., Morais-Cabral, J. H., *et al. Nature* **414**, 43-48 (2001).

117. Gouaux, E. and MacKinnon, R. *Science* **310**, 1461-1465 (2005).

118. Eijkel, J. C. T. and van den Berg, A. *Microfluid. Nanofluid.* **1**, 249-267 (2005).

119. Sparreboom, W., van den Berg, A., *et al. Nat. Nanotechnol.* **4**, 713-720 (2009).

120. Duan, C. H. and Majumdar, A. *Nature Nanotechnology* **5**, 848-852 (2010).

121. Beckstein, O., Tai, K., *et al. J. Am. Chem. Soc.* **126**, 14694-14695 (2004).

122. Richards, L. A., Schäfer, A. I., *et al. Small* **8**, 1701-1709 (2012).

123. Thompson, A. N., Kim, I., *et al. Nat. Struct. Mol. Biol.* **16**, 1317-U1143 (2009).

124. Jensen, M. O., Borhani, D. W., *et al. Proc. Natl. Acad. Sci. U. S. A.* **107**, 5833-5838 (2010).

125. Lauw, Y., Horne, M. D., *et al. Phys. Rev. Lett.* **103**, 117801 (2009).

126. Borukhov, I., Andelman, D., *et al. Phys. Rev. Lett.* **79**, 435-438 (1997).

127. Levin, Y. *Phys. Rev. Lett.* **102**, 147803 (2009).

128. Skinner, B., Loth, M. S., *et al. Phys. Rev. Lett.* **104**, 128302 (2010).

129. Boström, M., Williams, D. R. M., *et al. Phys. Rev. Lett.* **87**, 168103 (2001).

130. Cansado, I., Gonçalves, F., *et al. Carbon* **45**, 2454-2455 (2007).

131. Cansado, I. P., Gonçalves, F., *et al. Fuel Process. Technol.* **90**, 232-236 (2009).

132. McNicholas, T. P., Wang, A., *et al. J. Phys. Chem. C* **114**, 13902-13908 (2010).

133. Anderson, R. J., McNicholas, T. P., *et al. J. Am. Chem. Soc.* **132**, 8618-8626 (2010).

134. Ilott, A. J., Trease, N. M., *et al. Nature communications* **5** (2014).

135. Wang, H., Köster, T. K. J., *et al. J. Am. Chem. Soc.* **133**, 19270-19273 (2011).

136. Deschamps, M., Gilbert, E., *et al. Nature materials* (2013).

137. Wang, H.-J., Kleinhammes, A., *et al. J. Phys. Chem. C* **118**, 8474-8480 (2014).

138. Forse, A. C., Griffin, J. M., *et al. J. Phys. Chem. C* **118**, 7508–7514 (2014).

139. Xing, Y.-Z., Luo, Z.-X., *et al. Carbon* **77**, 1132-1139 (2014).

140. Slichter, C. P., *Principles of magnetic resonance*. (Springer Science & Business Media, 1990).

141. Abragam, A. *Oxford: University Press* **119**, 120 (1999).

142. Levitt, M. H., *Spin dynamics: basics of nuclear magnetic resonance*. (John Wiley & Sons, 2001).

CHAPTER 2 PROBING CARBON MICROPORES BY NUCLEUS INDEPENDENT CHEMICAL SHIFT

An accurate determination of the PSD of activated carbon is a challenging problem, especially for the subnanometer-sized micropores. Here, a simple room temperature method is introduced for determining the PSD of activated carbons based on the ^{1}H MAS NMR spectrum of adsorbed water. The observed NMR chemical shift is determined by the NICS mechanism. A DFT computation of the NICS yields a quantitative relationship between the observed chemical shift and the micropore size. This relationship provides a direct link between the lineshape of the ^{1}H MAS spectrum and the PSD.

2.1 Introduction

Activated carbons (ACs) are widely used in many applications such as water treatment, chemical purification, catalysis, and energy storage devices [1]. All these applications depend strongly on the porous structure of carbons characterized by a complex network consisting of micropores (< 2 nm), mesopores (2 ~ 50 nm), and macropores (> 50 nm)[2]. In particular, the micropore network with characteristic pore sizes below 2 nm plays a crucial role. The adsorption isotherm measurement is the conventional approach to characterize the PSD. Among the probe molecules (He, Ar, N_2, CO_2, H_2O etc.), the N_2 adsorption at 77 K is the most frequently used for ACs' characterization [3]. Several theoretical models are employed to interpret such adsorption isotherms and to derive the surface area and PSD. Here, the most well-known is the Brunauer-Emmett-Teller (BET) equation for the interpretation of the N_2 adsorption isotherm. However,

this method fails in micropores where the micropore filling is an important adsorption mechanism but it violates the assumptions of the BET theory [2].

Alternative methods such as the Dubinin-Stoeckli equation [4] have also been proposed to determine the PSD of micropores. However, this equation is semi-empirical. It is based on the assumption of a Gaussian PSD and requires the knowledge of the binding energy [4]. Recently, the relationship between N_2 or Ar isotherms and the pore size has been predicted using the DFT [5-7]. This method needs information on the interaction potentials and requires isotherms measured at extremely low relative pressure $P/P_0<10^{-5}$ (P_0 is the saturated vapor pressure) which is very time consuming. Besides the adsorption isotherm measurements, several other methods for characterizing the PSD of ACs have also been introduced, including the NMR cryoporometry [8], relaxometry [9], and diffusometry [10]. However, complicated experimental methods and techniques are required in these approaches.

Simple characterization methods are highly desirable for a convenient and reliable measurement of carbon PSDs in the micropore range. Here, a novel method is introduced to characterize the PSD by taking a room temperature ^{1}H MAS NMR spectrum of a known quantity of water added to the AC sample. This approach is made possible by a DFT calculation of the NICS [11], which establishes a quantitative relationship between the micropore size and the NICS in ACs. This method is applicable to samples with graphite-like local internal surfaces which can produce a NICS. It only requires taking one ^{1}H MAS spectrum of the water/carbon mixture and involves no additional knowledge such as the interaction potentials or adsorption mechanisms.

2.2 Experimental Details and DFT Calculation

2.2.1 Sample Preparation

The high temperature polymer PEEK was used to prepare the ACs by a method slightly modified from the previously reported procedure [12]. The sample preparation process is divided into two steps: carbonization and activation. The carbonization process creates very small micropores and provides seeds for further micropore growth upon activation. The activation process enlarges the micropores by a high temperature H_2O vapor reacting with the weak bonds in the carbonized sample. During the carbonization, 1 g of granulated Victrex® PEEK™ was placed in the center of a tubular furnace and heated under argon flow to 900 ℃ with a ramp rate of 45 ℃/min. After 30 min at 900 ℃, the carbonized chunks were cooled down to room temperature under argon flow and then ground into fine particles of approximately 0.5 mm in diameter. The ground material was heated up again to 900 ℃ and activated under the water vapor carried by the Ar gas flow for a chosen time period before cooling down to room temperature. A longer time activation leads to a larger micropore size and a larger burn-off value (BO), which is defined as the ratio of the mass reduction during the activation step to the sample mass before the activation but after the carbonization: $\mathrm{BO} = (m_c - m_a)/m_c$, where m_a is the mass after the activation and m_c is the mass before the activation but after the carbonization. The PEEK precursor loses approximately 50% of its mass in the carbonization step. The activated carbon sample is labeled based on its BO value, for instance, P-92 represents an AC sample with a BO value of 92%. Here "P" represents the precursor PEEK. Figure 2.1 is a transmission electron microscope (TEM) image of the P-92 AC sample.

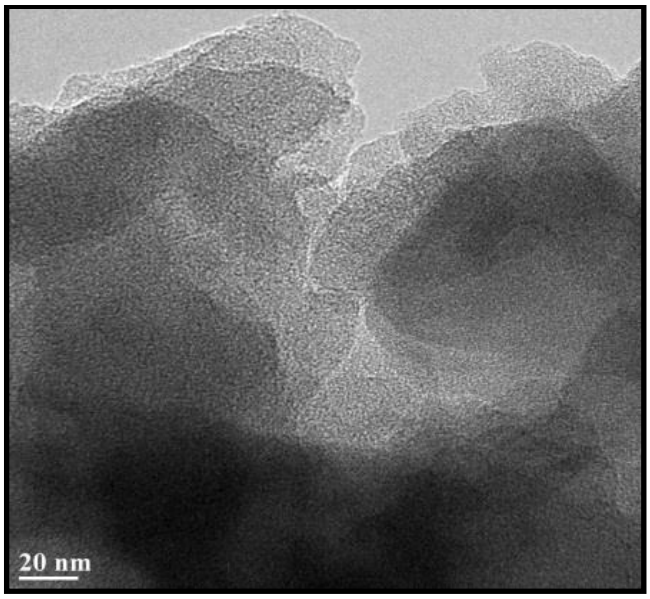

Figure 2.1: TEM image of a carbon sample with BO = 92% activated at 900 ℃.

2.2.2 NMR Experiment

The ^{1}H MAS NMR spectrum was recorded on a 9.4 T magnet (400 MHz for ^{1}H) with a TECMAG APOLLO spectrometer and a Chemagnetics 4mm MAS probe. About 10 mg carbon powder was loaded into the MAS rotor with an air tight O-ring plug. The ^{1}H spectrum was acquired at a spinning speed of 8 kHz (all NMR spectra in this chapter were taken under 8 kHz MAS unless otherwise specified). A background ^{1}H MAS spectrum of the dry sample stored in a desiccator was first recorded. It had a weak featureless broad peak of 60 ppm, containing about 4×10^{20} protons/gram, and was subtracted from all the spectra presented in this chapter. After that, a known amount of distilled water was injected into the sample-containing MAS rotor using a syringe. Water was adsorbed in the micropores immediately after the injection and the sealed sample reached equilibrium in less than 5 min as monitored by the NMR spectra. The amount of water added to the AC sample was determined both by the volume of injected water and by measuring the weight change of the MAS rotor. To verify the reversible water adsorption in the

micropores, the sample was dried in a desiccator for 48 hours after the NMR experiment and the background spectrum was taken again. The two background spectra (before adding water and after drying in a desiccator) were identical, indicating that no permanent chemical bonds are formed in the process of the experiment. The water loading was also implemented by placing AC samples in a saturated water vapor at room temperature for 20 hours. The ^{1}H MAS spectra of water loading by the vapor adsorption and by the liquid injection were compared.

2.2.3 DFT Calculation Approach

All the DFT computation results were obtained using Gaussian 09-b01 [13]. The internal surface structure of ACs was mimicked by the central carbon ring of the circumcoronene molecule (shown in Figure 2.2). The circumcoronene structure was optimized at the B3LYP/6-311G(d) level [14]. The NICS was computed by the Gauge-Independent Atomic Orbital (GIAO) method [15-19]. The ghost atom [20] used to probe the NICS was placed at three different locations in the center ring, namely, above the ring center, above the carbon atom and above the C-C bond center, as illustrated in Figure 2.2. At each location, the NICS value was evaluated as a function of the distance to the carbon surface.

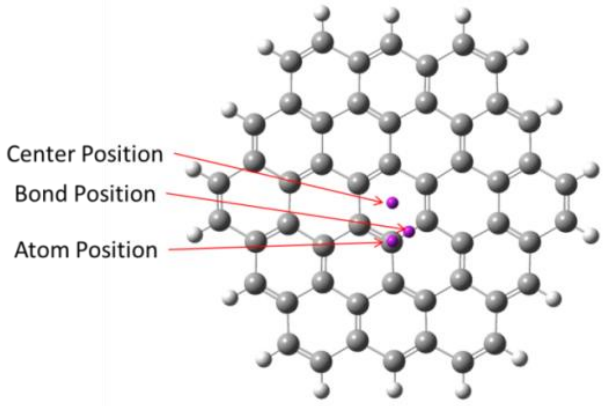

Figure 2.2: The molecular structure of circumcoronene and the three locations of the ghost atom (purple dots).

2.2.4 Chemical Shift Mechanism in AC Micropores

The chemical shift mechanism resulting from the interatomic ring current, such as that of a benzene molecule [21], has been recognized for a long time [22,23]. The diamagnetic response of the cyclic conjugated π electrons in benzene to the applied magnetic field leads to an upfield chemical shift [21,23]. This effect has been observed in ^{1}H NMR spectra for several different adsorbates, such as hydrogen [24], water [25], ammonia [26] and others, on the surface of aromatic systems. Since the chemical shift is due to the diamagnetic and paramagnetic effects of the ring current associated with the aromatic and anti-aromatic compound, it is independent of the probe atom. An upfield NICS value indicates the existence of a diatropic ring current [27]. Therefore the so-called NICS index is widely used for characterizing the aromaticity and antiaromaticity [11,27,28].

As expected, there is also a large NICS effect in ACs. Figure 2.3 shows the static ^{1}H, ^{19}F, and ^{23}Na spectra of a 1M $NaBF_4$ aqueous solution injected into a P-40 sample. Two well-resolved peaks are clearly observed in all three spectra. The left peak of the ^{1}H spectrum, peak A, is due to the water stored in large mesopores and/or macropores. It is slightly shifted upfield by 0.1 ppm compared to that of the bulk water due to the isotropic bulk magnetic susceptibility effect. Since the whole sample experiences the identical isotropic bulk magnetic susceptibility effect, it is suitable to use peak A as a reference for measuring the NICS value. Setting the chemical shift of the left peak as 0 ppm for all three nuclei, the right peaks, peak B, on all three spectra exhibit the same chemical shift of -7.7 ppm. Peak B is associated with the water adsorbed inside the micropores [25]. The upfield shift of peak B with respect to peak A is due to the NICS effect [21-23]. It is not related to any effect of chemical bonding since all three nuclei exhibit the same chemical shift.

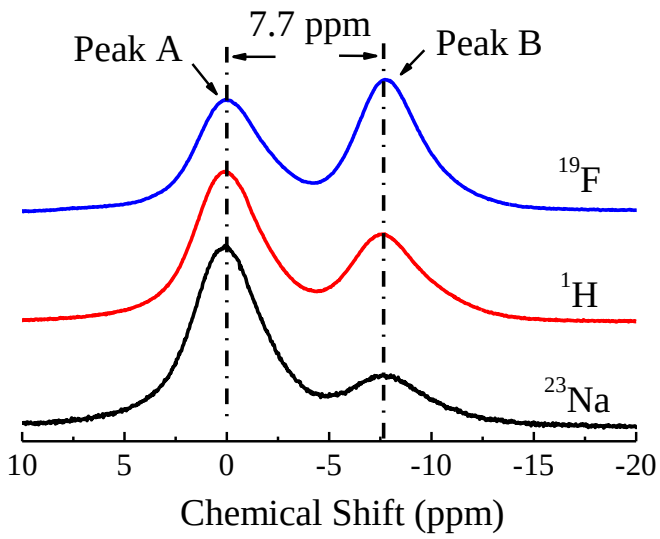

Figure 2.3: Static ^{1}H, ^{19}F, ^{23}Na spectra of a P-40 AC sample filled with 1 M $NaBF_4$ solution. The left peak (peak A) is set as the reference (0 ppm) and the right peaks (peak B) of all three nuclei exhibit the same chemical shift of -7.7 ppm due to the NICS effect.

2.2.5 DFT Calculation of NICS

The NICS value as a function of the distance between the probe atom and the carbon surface (carbon atom center), $\delta(r)$, can be obtained from the DFT calculation [29]. Here the central carbon ring of the circumcoronene molecule is used to model the carbon micropore surface (Figure 2.2). The shielding tensor of the NICS can then be calculated using the DFT method at the position specified by the NICS probe atom. The calculation result of $\delta(r)$ is shown in Figure 2.4a. The NICS at three different locations, namely, above the ring center, above the carbon atom and above the C-C bond center, are nearly identical when the distance *r* is larger than 0.32 nm. Since the water molecule cannot approach the surface closer than this distance, $\delta(r)$ is assumed to be independent of the horizontal position on a graphitic surface. For the convenience of calculation, $\delta(r)$ is fitted empirically in the region $0.3\ \text{nm} \le r \le 3.0\ \text{nm}$ with a stretched exponential function $\delta(r) = A\exp\left[-(r/r_0)^{\beta}\right]$. An excellent fitting is obtained

with the parameter $A = 24.6 \pm 1.2$ ppm, $r_0 = 0.23 \pm 0.01$ nm, and $\beta = 0.75 \pm 0.02$ as shown in Figure 2.4a.

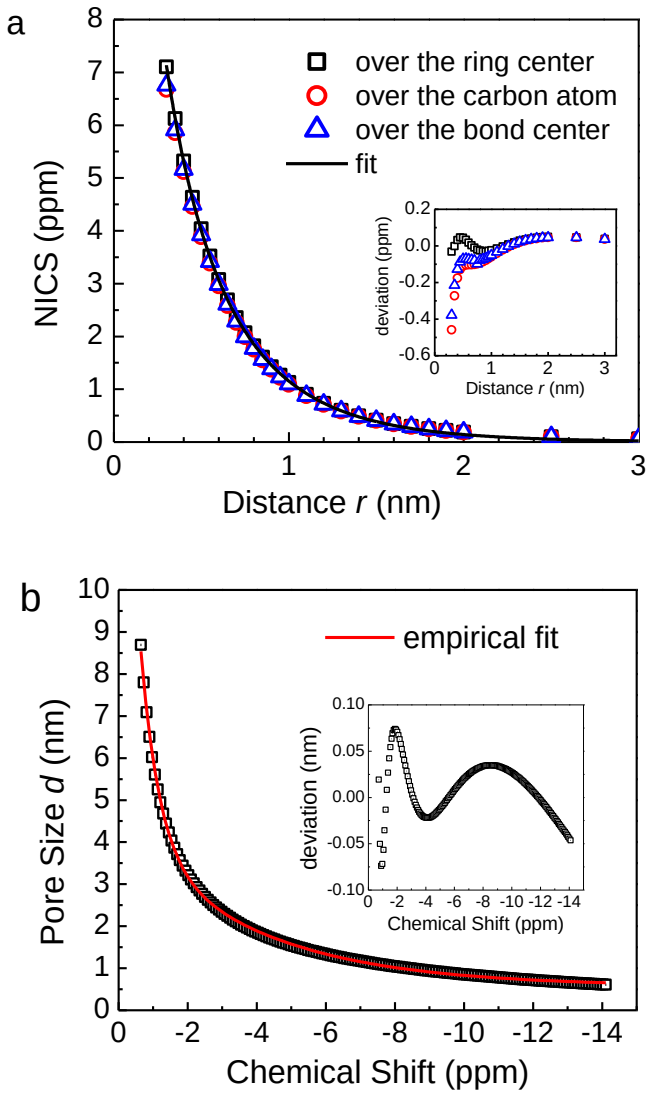

Figure 2.4: (a) The dependence of the NICS on the distance from the molecule to the surface obtained by a DFT calculation. Three probe atom locations are used: over the ring center, over the carbon atom, and over the bond center of the central carbon ring of circumcoronene. The solid line is an empirical fit of the numerical $\delta(r)$ with $\delta(r) = A\exp\left[-(r/r_0)^{\beta}\right]$. The inset shows the difference between the DFT calculation and the fit. (b) The relationship between the pore size *d* (atom center to center for a slit-shaped pore) and the averaged NICS δ_{avg} deduced from Eq. (2.2). The solid line is an empirical fit of the numerical result with Eq. (2.3). The inset shows the difference between the values from Eq. (2.2) and Eq. (2.3).

2.2.6 NICS Averaging in Slit-Shaped Pores

A simple exchange model is assumed to correlate the NICS-related isotropic chemical shift with the pore size. As shown in Figure 2.5, inside a slit-shaped pore [30], water molecules are distributed throughout the internal space of the micropores. On the NMR timescale of 10 ms, a water molecule can explore all the nanopore space because of its fast translational motion. Since the NICS is a function of the distance from the molecule to the surface, as shown in Figure 2.4a, the measured NICS-related isotropic chemical shift of a fully filled micropore is the NICS averaged over the pore space and can be calculated as

$$\delta_{avg}(d) = \frac{\int_{w}^{d-w} \delta(r)\,dr}{\int_{w}^{d-w} dr} + \frac{\int_{w}^{d-w} \delta(d-r)\,dr}{\int_{w}^{d-w} dr} = 2\frac{\int_{w}^{d-w} \delta(r)\,dr}{\int_{w}^{d-w} dr} \tag{2.1}$$

where δ_{avg} is the averaged NICS, d is the pore width (from carbon center to carbon center) of the slit-shaped pore, and w, chosen as 0.32 nm [24], is the closest distance between the water hydrogen and the carbon layer. The NICS contributions from both the carbon surfaces are taken into account in Eq. (2.1).

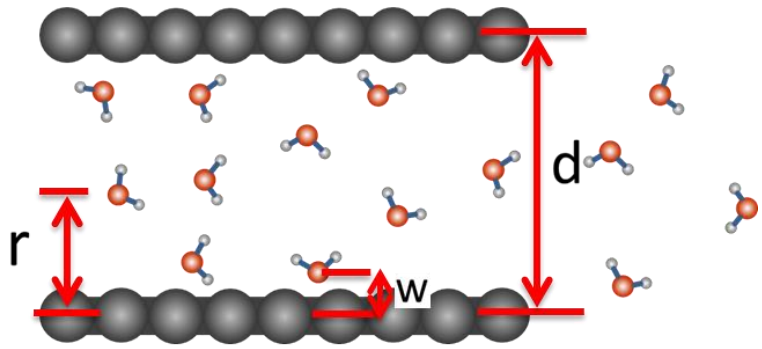

Figure 2.5: Illustration of water molecules inside a slit-shaped pore of width d (carbon center to carbon center). w is the closest distance that water molecules can approach the surface.

2.2.7 Correlation between the Pore Size and the Chemical Shift

By plugging $\delta(r) = A\exp\left[-(r/r_0)^{\beta}\right]$ into Eq. (2.1), the averaged NICS value, δ_{avg}, can then be calculated as a function of the pore size *d* by

$$\delta_{avg}(d) = \frac{2A}{d-2w}\int_{w}^{d-w} e^{-(r/r_0)^{\beta}}\,dr \tag{2.2}$$

The function in Eq. (2.2) can be inverted numerically to obtain the dependence of the pore size *d* on δ_{avg} and this numerical result is shown in Figure 2.4b. Again, for the convenience of future usage, the numerical result of *d* versus δ_{avg} is fitted empirically with the following function

$$d = A_1\exp\left(-\delta_{avg}/\delta_1\right) + A_2\exp\left(-\delta_{avg}/\delta_2\right) + d_0 \tag{2.3}$$

The fitting parameters are $A_1 = 16.1 \pm 0.2$ nm, $\delta_1 = -0.531 \pm 0.008$ ppm, $A_2 = 3.83 \pm 0.05$ nm, $\delta_2 = -3.75 \pm 0.06$ ppm and $d_0 = 0.57 \pm 0.01$ nm. As shown in Figure 2.4b, an excellent fit is achieved. Figure 2.4b shows that the water contained in the mesopores larger than 3 nm produces a NICS value less than 2 ppm, which will contribute to peak A rather than peak B due to its exchange with the intergranular water. Peak B corresponds to the water contained in the micropores ($d \le 2$ nm).

A complete micropore filling is important for the application of this model, especially for large micropores. Figure 2.6a compares the ^{1}H MAS NMR spectrum of a P-0 sample with water adsorbed under saturated water vapor pressure for 20 hours with that by liquid water injection. After 20 hours exposure to the saturated water vapor, the mass ratio of the adsorbed water to P-0 is 0.19. Its spectrum shows a single peak B and the water is only adsorbed into the micropores. The AC external surface is hydrophobic therefore no significant water condensation occurs. The

internal surfaces of all the accessible micropores have a graphite-like surface structure, giving rise to a nearly identical NICS. Further water injection with a syringe increases the water to AC mass ratio from 0.19 to 0.39. At this point, peak A emerges, but peak B remains the same. This indicates that the micropores are already fully filled with water during the 20-hour exposure to the saturated water vapor. The additional water injected only goes to the large mesopores and/or macropores, giving rise to peak A. For comparison, liquid water is injected into a dry P-0 AC sample directly and the spectrum (Figure 2.6a) shows an identical peak B with that after 20-hour exposure to the saturated water vapor. Thus, the water injection method also results in fully filled micropores.

Figure 2.6b shows the ^{1}H MAS NMR spectra of a P-92 AC sample filled with different amount of water by the liquid water injection using a syringe. Here, peak B appears first and grows in intensity as the amount of adsorbed water increases. After the mass ratio of water to carbon reaches 1.42, peak A starts to emerge while peak B stops growing. It is noticed that in Figure 2.6b, peak B shifts gradually toward a smaller NICS value as its intensity increases with increased water filling. A 0.7 ppm chemical shift difference is observed between the spectra of partially filled and fully filled P-92. When a small amount of water is initially added into the micropores, water molecules are preferentially adsorbed on the surface and spend, on average, more time near the surface where the NICS effect is large. With more water added, the pore space is gradually filled up and the water distribution averaged over time is close to the volume average used in Eq. (2.1). Therefore, the measured NICS-related isotropic chemical shift (shift of peak B with respect to the shift of peak A) of a fully filled micropore would have a less negative value (lower field) compared to that of a partially filled micropore, as shown in Figure 2.6b.

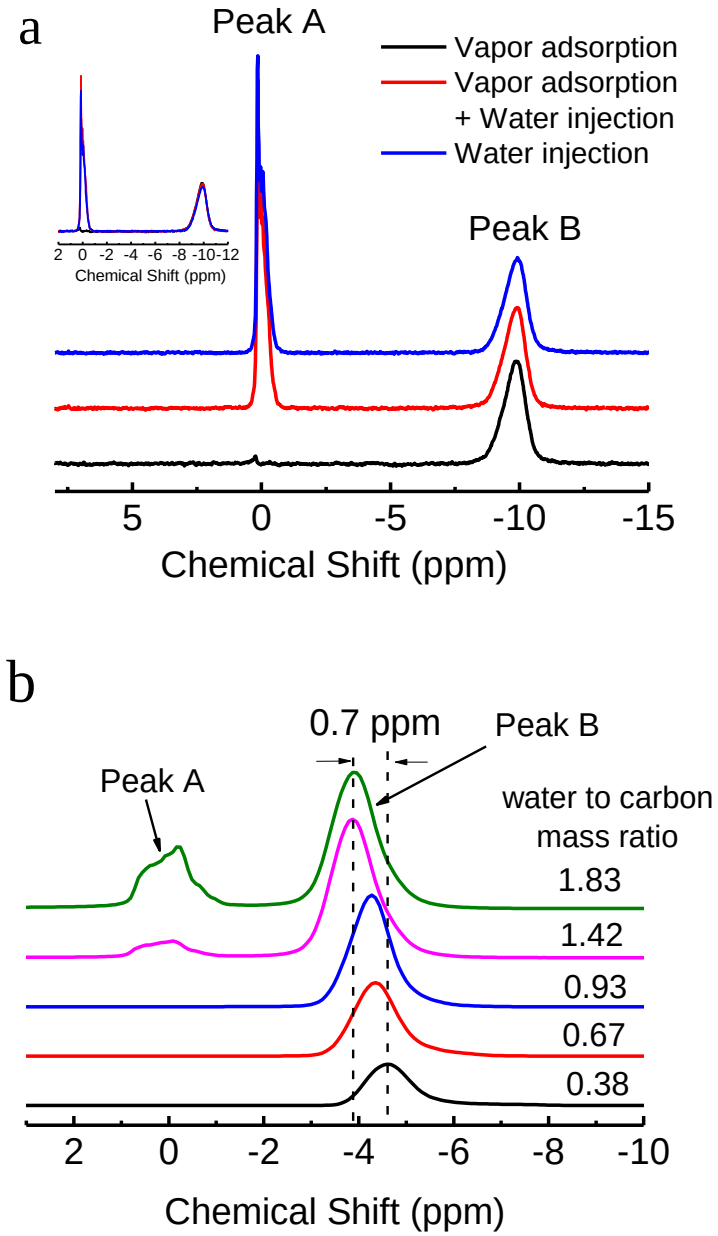

Figure 2.6: (a) ^{1}H MAS spectra of water in a P-0 AC sample with different water filling methods: Adsorption in saturated water vapor pressure (black), vapor adsorption followed by liquid water injection (red); liquid water injection by a syringe (blue). The inset shows the overlay of the three spectra. The identical peak B indicates that the micropores are fully filled by each method. (b) ^{1}H MAS spectra of water in a P-92 AC sample at different water filling level with water/carbon mass ratio ranging from 0.38 to 1.83. The chemical shift of peak B at low filling level (0.38) differs by 0.7 ppm from that of fully filled micropores (mass ratio 1.42 and above). There are some sharp peaks in peak A, which are probably due to water in mesopores or intergranular space that are resolved under MAS.

2.2.8 Micropore Volume

The amount of water adsorbed inside the micropores can be measured quantitatively by the NMR and can be used to calculate the micropore volume. Since the ^{1}H MAS NMR spectra clearly resolve the peak associated with the water in the micropores from the peak associated with the water outside, the amount of water inside the micropores can be easily determined from the known amount of the added water and the ratio of peak B intensity versus the total spectral intensity. The total micropore volume per unit mass of AC sample, V_B / m_s, can be calculated by

$$\frac{V_B}{m_s} = \frac{1}{\rho_w} \cdot \frac{A_B}{A_{total}} \cdot \frac{m_w}{m_s} \tag{2.4}$$

where m_w and m_s are the water mass and the AC sample mass, respectively, $\rho_w = 0.9$ g/cm^3 is the water density in micropores [31], A_{total} is the total spectral intensity, and A_B is the intensity of peak B.

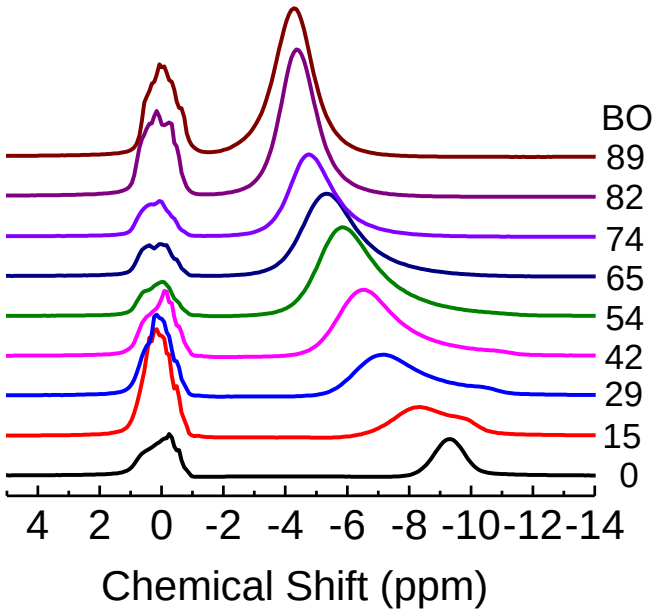

Figure 2.7: ^{1}H MAS spectra of water-filled AC samples. BO values are indicated in the figure.

After the pore size *d* as a function of δ_{avg} being established, it is straightforward to calculate the dominant pore size of the micropores in an AC sample using the chemical shift of peak B. The ^{1}H spectra of water-filled ACs samples with different BO values are shown in Figure 2.7. Table 2.1 summarizes the information extracted from the spectra including the measured δ_{avg} and the corresponding pore size *d*, as well as the micropore volume and the micropore surface area. The pore size defined as the surface to surface distance is determined by $d^* = d - 0.34\ \text{nm}$ where the carbon atom diameter, 0.34 nm, is taken from the solid-solid Lennard-Jones interaction parameter [32]. The micropore internal surface area is calculated from the pore volume and the pore width d^* by

$$S = \frac{2V_B}{m_s \cdot d^*} \tag{2.5}$$

The 92% and 0% BO AC samples are also characterized by the nitrogen adsorption isotherms (Figure 2.8). The typical Type I adsorption isotherm indicates that the dominant pore type is the micropore. The BET area (5 points fitting at the relative pressure range from 0.05 to 0.3) and the total pore volume of the 92% BO sample are $2888\ \text{m}^2/\text{g}$ and 1.55 cm^3/g, respectively. The 0% BO sample has $0.18\ \text{cm}^3/\text{g}$ total pore volume. The micropore volume calculated by the MAS NMR method agrees very well with the nitrogen adsorption method in both the 92% and 0% BO samples as shown in Table 2.1. As discussed in section 2.3.4, the internal surface of all accessible micropores has graphite-like structure, thus the specific surface area (SSA) of the AC samples should be smaller than the theoretical SSA of graphene (2360 m^2/g). Therefore, the SSA of the 92% BO sample calculated by the present method ($1912\ \text{m}^2/\text{g}$) is quite reasonable.

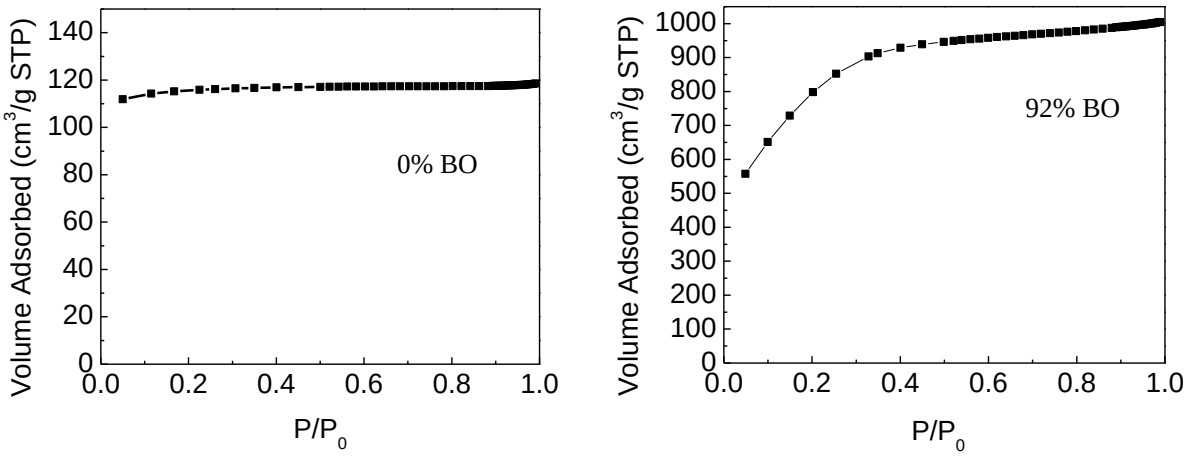

Figure 2.8: Nitrogen gas adsorption isotherms of 0% BO and 92% BO AC samples. P/P_0 in the *x*-axis is the relative pressure of nitrogen gas at 77K.

Table 2.1: The MAS NMR characterization of AC samples with different BO values. The chemical shift of peak B is referred to water ^{1}H outside the nanopores. *d* is the carbon pore size from carbon center to carbon center assuming a slit-shaped pore. $d^*= d$-0.34 nm is the effective pore size from carbon surface to carbon surface.

BO(%)	^{1}H peak B center (ppm)	Pore size *d* (nm)	Pore size d^* (nm)	Micropore Volume (cm^3/g)	Micropore surface area (m^2/g)
0	-9.3	0.92	0.58	0.19	642
15	-8.3	1.02	0.68	0.25	747
29	-7.2	1.15	0.81	0.38	928
42	-6.5	1.25	0.91	0.51	1117
54	-5.8	1.38	1.04	0.67	1290
65	-5.3	1.47	1.13	0.88	1553
74	-4.8	1.59	1.25	1.00	1603
82	-4.4	1.71	1.37	1.18	1719
89	-4.3	1.74	1.40	1.39	1992
92	-3.9	1.89	1.55	1.48	1912

2.2.9 Peak Broadening and PSD

Compared with the static spectra, the full width at half maximum (FWHM) of the ^{1}H spectrum under MAS is significantly reduced from 4.6 ppm to 1.3 ppm, as shown in Figure 2.9.

Although the peaks of both the static and MAS spectra have the same average chemical shifts, the large anisotropic broadening in the static spectra obscures the contribution of the intrinsic NICS distribution associated with the PSD. In the MAS spectra, the anisotropic broadening is removed [33] and the linewidth of peak B is dominated by the PSD. The transverse relaxation time T_2 under MAS is about 6 ms, which contributes to an intrinsic line broadening of 0.13 ppm. This is much smaller compared to the observed FWHM of 1.3 ppm, indicating that the peak width is mainly determined by the NICS distribution. Therefore, it is possible to derive the PSD from the MAS spectrum.

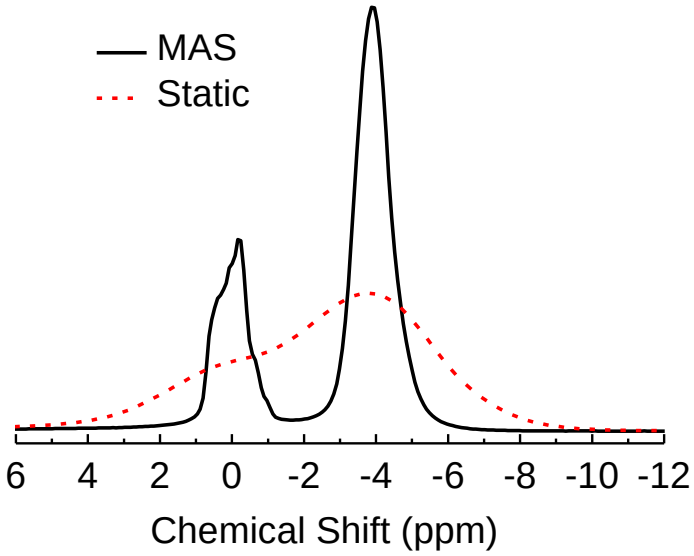

Figure 2.9: The ^{1}H spectra of water in a P-92 AC sample. The static spectrum (dashed line, red) has a FWHM of 4.6 ppm and the MAS spectrum (solid, black) has a FWHM of 1.3 ppm.

The function of the pore volume versus the pore size, $V(d)$, is needed to calculate the PSD. The pore volume distribution function $V(d)$ can be calculated from the MAS NMR lineshape $I(\delta)$ by

$$V = \int V(d)\mathrm{d}d \propto \int I(\delta)\mathrm{d}\delta(d) = \int I(\delta)\delta'(d)\mathrm{d}d \qquad (2.5)$$

Therefore, $V(d) \propto I(\delta)\delta'(d)$. This relates the PSD, $V(d)$, to the MAS NMR lineshape $I(\delta)$ and the chemical shift-pore size relationship $\delta'(d)$, where $\delta'(d)$ can be obtained directly by taking the derivative of the function in Eq. (2.2) with respect to *d*. The NMR spectra in Figure 2.7 can then be transformed into the PSDs, which are shown in Figure 2.10. The distribution is scaled so that the area under the curve is proportional to the total pore volume listed in Table 2.1.

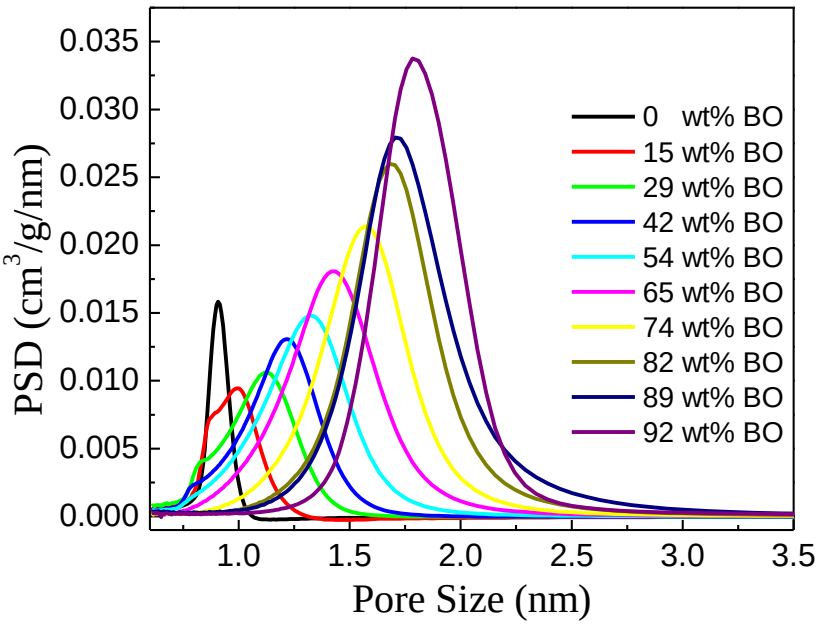

Figure 2.10: The PSDs obtained from the ^{1}H MAS NMR spectra. As the BO value increases, the average pore size and the PSD increases. For the 15 BO and 29 BO samples, the pore size is not very uniform because the activation extent is not the same for the interior and the edge of an PEEK particle.

Since the NICS effect is a local effect, it does not require the surface to be graphite-like continuously over a large scale. It is important to realize that the NICS NMR porometry technique is not an atomic-scale structural imaging technique. It probes the local structure averaged over a certain length scale and measures the average pore size over that length scale. The carbonization temperature is a crucial parameter in the sample preparation for making the surface locally graphite-like. All the AC samples discussed in this work are carbonized at 900 ^{o}C.

Graphitic crystalline domains can be clearly observed in the TEM image for samples carbonized at a temperature above 1000 ^{o}C (Figure 2.11). High carbonization temperature makes the atomic hybrid orbital predominantly sp^2-like rather than sp^3-like, and makes the graphite-like domain larger. The structural model employed for the NICS calculation is circumcoronene. A larger graphite-like domain could give rise to a slightly larger (on the order of 1 ppm [29]) NICS effect. This would give rise to an uncertainty in the determined pore size of approximately 0.08 nm (or 8%) for an average pore size of 1 nm (carbon atom center to center) and 0.36 nm (or 18%) for an average pore size of 2 nm (carbon atom center to center).

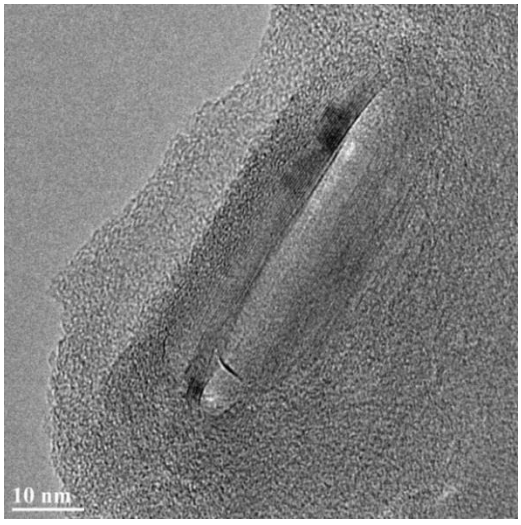

Figure 2.11: A TEM image of a 0% BO sample carbonized at 1100 ^{o}C. Graphitic crystalline domains can be clearly observed.

As mentioned above, the NMR porometry based on the NICS measures the average pore size over a certain length scale. This length scale of the averaging is determined by the diffusion length *l* of the probing molecule (H_2O in the current experiment) over the NMR time scale (T_2^*), which is about 600 μs in the activated carbon system. Since the diffusion coefficients of water molecules and BF_4^- ions inside the AC micropores are on the order of $10^{-10}\ m^2/s$ [34,35] and

$10^{-12}\ m^2/s$ [36] respectively, the estimated diffusion range during the NMR time scale is about 600 nm for water and 60 nm for BF_4^-.

Figure 2.12 compares the lineshape of the ^1H and ^{19}F spectra. The spectra are scaled to have a similar intensity in peak B for the convenience of lineshape comparison. As we can see, ^1H and ^{19}F have very similar lineshape except for the small hump on the right shoulder of the ^1H spectrum. This is due to some small micropores that are accessible to water but not to the BF_4^- ions. The similar lineshape between ^1H and ^{19}F spectra indicates that the length scale of the averaging in the NICS NMR porometry technique is around 60 nm or less. The diffusion of water molecules can be restricted within micropores by barriers such as the pore throats. As it was reported [37], when the probe molecules enter the micropore space, they tend to stay in this space and the diffusion coefficient of the probe molecules confined inside the AC micropores can be very small ($4\times10^{-13}\,m^2/s$ for ethanol) and the length scale of averaging can be even smaller than 60 nm.

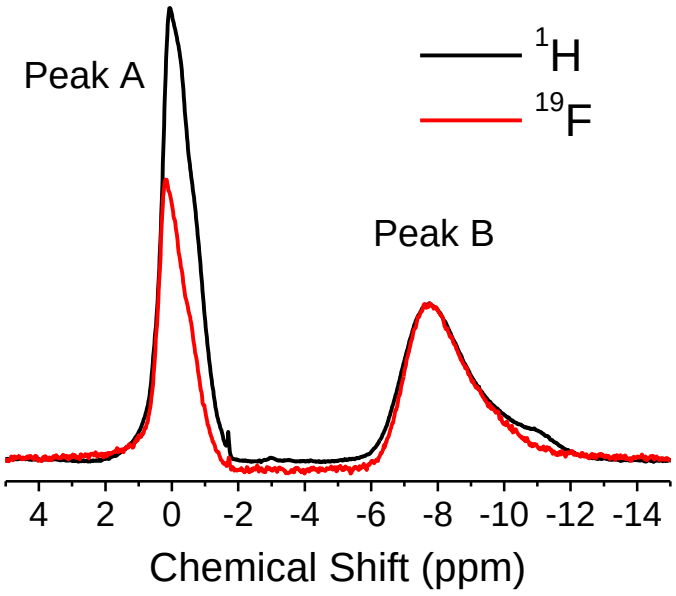

Figure 2.12: ^1H, ^{19}F MAS spectra of a P-32 AC sample filled with 1M $NaBF_4$ solution.

Nevertheless, the PSD measured by the NICS NMR porometry is a course-grained one over the length scale of the diffusion averaging. In the AC samples where micropores and mesopores are mixed in a very short length scale, for example, less than l0 nm, the NICS NMR porometry would then provide a pore size averaged over the micropores and the mesopores. In this case, peak B will merge with peak A and this could occur in the samples with a very high BO value [24]. Figure 2.13 compares the water ^{1}H spectra in P-89 and P-94 AC samples. There is clearly a qualitative change in the ^{1}H spectrum of P-94 AC sample. Here, peak B nearly collapses and merges with peak A. The high degree of activation creates a lot of open structures where water molecules can effectively go through the micropores and the mesopores over the time scale of T_2^*, causing the merging of peak A and peak B. This averaging effect gives rise to a seemingly smaller micropore volume in P-94 even though the BO value is higher. In this case, the present technique is no longer effective for a quantitative pore structure characterization.

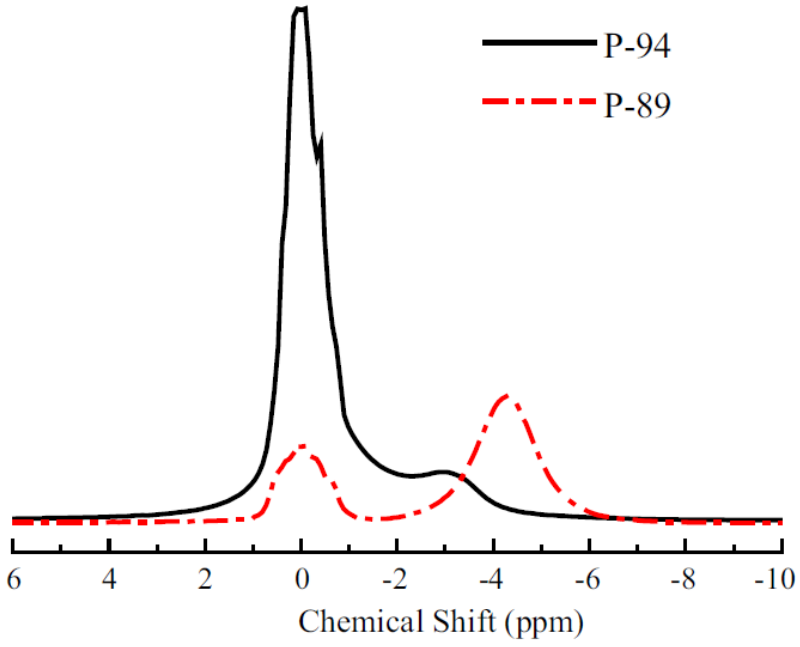

Figure 2.13: The ^{1}H spectra of water in P-89 (dash-dotted line) and P-94 (solid line) AC samples. The intensity (spectral area) is scaled by the water/AC mass ratio.

2.3 Conclusions

NMR is a powerful tool for studying porous media. The NICS NMR porometry technique introduced here is suited for investigating activated carbons with pore size smaller than 2 nm, a challenging pore size range for traditional characterization methods. This simple technique offers information on the pore size, PSD, pore volume, and surface area. It is based on a room temperature ^{1}H MAS NMR spectrum of H_2O adsorbed in the carbon micropores. Because of the NICS effect, a distinct chemical shift is identified for H_2O molecules adsorbed inside the micropores. The total micropore volume of the ACs can be calculated from the intensity of the peak associated with water in micropores and the total amount of water added to the sample. A straightforward relationship between the PSD and the lineshape of the MAS NMR spectrum is established, allowing the determination of the PSD from the lineshape of the ^{1}H MAS NMR spectrum. All these are made possible by DFT calculations which establish the function of the NICS versus the distance between the probe atom and the graphitic surface. It is expected that this function is widely applicable for materials with local surface structures similar to a graphitic surface, so the only remaining task in the future usage of this method is to take a room temperature ^{1}H MAS spectrum with a known quantity of water added to the sample. From this, the micropore size distribution can be derived in a straightforward way.

2.4 REFERENCES

1. *Nanoporous materials : science and engineering*. (Imperial College Press; Distributed in the US by World Scientific Publishing, London; Hackensack, 2004).

2. Sing, K. S. W., Everett, D. H., *et al. Pure Appl. Chem.* **57**, 603-619 (1985).

3. Rodriguez-Reinoso, F. and Molina-Sabio, M. *Adv. Colloid Interface Sci.* **76**, 271-294 (1998).

4. Hutson, N. D. and Yang, R. T. *Adsorpt.-J. Int. Adsorpt. Soc.* **3**, 189-195 (1997).

5. Lastoskie, C., Gubbins, K. E., *et al. Journal of Physical Chemistry* **97**, 4786-4796 (1993).

6. Ryu, Z. Y., Zheng, J. T., *et al. Carbon* **37**, 1257-1264 (1999).

7. Ravikovitch, P. I., Haller, G. L., *et al. Adv. Colloid Interface Sci.* **76**, 203-226 (1998).

8. Gun'ko, V. M., Turov, V. V., *et al. Adsorpt.-J. Int. Adsorpt. Soc.* **17**, 453-460 (2011).

9. Krutyeva, M., Grinberg, F., *et al. Microporous Mesoporous Mat.* **120**, 91-97 (2009).

10. Furtado, F., Galvosas, P., *et al. Microporous Mesoporous Mat.* **141**, 184-191 (2011).

11. Schleyer, P. V., Maerker, C., *et al. Journal of the American Chemical Society* **118**, 6317-6318 (1996).

12. McNicholas, T. P., Wang, A. M., *et al. J. Phys. Chem. C* **114**, 13902-13908 (2010).

13. M. J. Frisch, G. W. T., H. B. Schlegel, G. E. Scuseria, , M. A. Robb, J. R. C., G. Scalmani, V. Barone, B. Mennucci, , *et al.*, Gaussian 09 (Gaussian, Inc., Wallingford CT, 2010).

14. R. Krishnan, J. S. B., R. Seeger, and J. A. Pople *The Journal of chemical physics* **72**, 5 (1980).

15. London, F. *J. Phys. Radium* **8**, 397-409 (1937).

16. McWeeny, R. *Physical Review* **126**, 1028-1034 (1962).

17. Ditchfie.R. *Mol. Phys.* **27**, 789-807 (1974).

18. Wolinski, K., Hinton, J. F., *et al. Journal of the American Chemical Society* **112**, 8251-8260 (1990).

19. Cheeseman, J. R., Trucks, G. W., *et al. J. Chem. Phys.* **104**, 5497-5509 (1996).

20. Stanger, A. *The Journal of Organic Chemistry* **71**, 883-893 (2006).

21. Pople, J. A. *J. Chem. Phys.* **24**, 1111-1111 (1956).

22. Jonathan, N., Dailey, B. P., *et al. J. Chem. Phys.* **36**, 2443-2448 (1962).

23. Pople, J. A. and Untch, K. G. *Journal of the American Chemical Society* **88**, 4811-4815 (1966).

24. Anderson, R. J., McNicholas, T. P., *et al. J. Am. Chem. Soc.* **132**, 8618-8626 (2010).

25. Dickinson, L. M., Harris, R. K., *et al. Magn. Reson. Chem.* **38**, 918-924 (2000).

26. Tabony, J. *Prog. Nucl. Magn. Reson. Spectrosc.* **14**, 1-26 (1980).

27. Lazzeretti, P. *Prog. Nucl. Magn. Reson. Spectrosc.* **36**, 1-88 (2000).

28. Gomes, J. and Mallion, R. B. *Chem. Rev.* **101**, 1349-1383 (2001).

29. Forse, A. C., Griffin, J. M., *et al. J. Phys. Chem. C* **118**, 7508–7514 (2014).

30. Texier-Mandoki, N., Dentzer, J., *et al. Carbon* **42**, 2744-2747 (2004).

31. Jensen, T. R., Østergaard Jensen, M., *et al. Phys. Rev. Lett.* **90**, 086101 (2003).

32. Steele, W. A., *The Interaction of Gases with Solid Surfaces*. (Pergamon Press, Oxford, New York, 1974).

33. H.Levitt, M., *spin dynamics*. (John Wiley&Sons, Ltd, Chichester, New York, Weinheim, Brisbane, Singapore, Toronto, 2001).

34. Liu, Y.-C., Wang, Q., *et al. Chemical physics letters* **381**, 210-215 (2003).

35. Kärger, J., D.M. Ruthven, and D. Theodorou, *Diffusion in zeolites and other nanoporous materials*. (Wiley-VCH, Weinheim, 2012).

36. Zuleta, M., Bjornbom, P., *et al. J. Electroanal. Chem.* **586**, 247-259 (2006).

37. Krutyeva, M., Grinberg, F., *et al. Microporous Mesoporous Mater.* **120**, 91-97 (2009).

CHAPTER 3 ELECTRONEUTRALITY BREAKDOWN AND SPECIFIC ION EFFECTS IN NANOCONFINED AQUEOUS ELECTROLYTES

In the previous chapter, a unique NMR method was established to identify nanoconfined molecules in activated carbons. Here I take advantage of this to selectively investigate various sodium salts aqueous electrolytes in nanoconfinement where the interfacial interactions play critical roles. Specifically, I study how the ion distribution in nanopores is affected by the nonelectrostatic interactions. This is a challenging problem that cannot be approached by other experimental techniques.

3.1 Materials and Methods

3.1.1 Nanoconfined Electrolytes Preparation

Similar to Chapter 2, the high quality nanoporous carbon derived from PEEK polymer was used to provide the hydrophobic nanoconfinement. Unless specified, all results discussed in this chapter were obtained on activated carbon P-40, which has an average pore size of 0.9 nm determined by the MAS NMR method introduced in the previous chapter. Activated carbon P-92 (average pore size 1.9 nm) was also used and was specified when it was encountered.

A series of sodium salts was purchased from Sigma-Aldrich and used as purchased without further purification. The purity is >99.0% expect for $NaBF_4$ (>98%). The aqueous electrolytes were prepared to contain 1 mol kg^{-1} Na^+ cations except for NaF (0.8 mol kg^{-1} because of its lower solubility in water). A simple procedure was followed for preparing the nanoconfined aqueous electrolyte. In general, 30 μL electrolyte was injected into 20 mg P-40 sample. The mixture was then tightly sealed in an NMR sample tube. P-40 has a pore volume of

0.5 cm^3 g^{-1} therefore 30 μL electrolyte is sufficient to fill the nanopores and about two thirds of the electrolyte is left in the intergranular space.

3.1.2 Static NMR on Uncharged P-40

The ^{1}H, ^{23}Na, ^{19}F (for NaF and $NaBF_4$), and ^{15}N (for $NaNO_3$, ^{15}N enriched) static spectra on the electrolyte/P-40 mixture were measured with a 400 MHz pulsed NMR system at room temperature (293 K). A single-pulse sequence was used for the measurement and the last delay was set long enough so that the signal was fully recovered after each scan. The acquisition of the FID signal was started at 5 μs after the 90 degree pulse. The 90 degree pulse of Na^+ inside the P-40 nanopores was shown to be the same as Na^+ in the intergranular space as well as in the pure aqueous electrolyte solution. In addition, there were no ^{23}Na sidebands under 7 kHz MAS. All these indicate that the quadrupole interaction effect is negligible here for the ^{23}Na NMR.

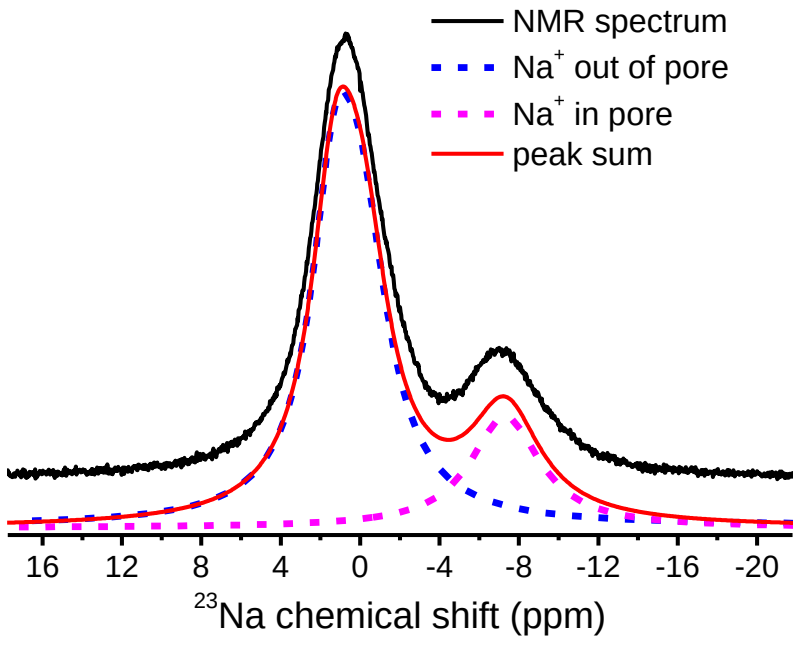

Figure 3.1: The deconvolution of ^{23}Na spectrum to obtain the intensities of ions inside and outside the nanopores.

To calculate the ion concentrations inside nanopores, the two peaks in the ^{23}Na NMR spectrum – representing ions in the nanopores and ions in the intergranular space, respectively – are deconvoluted to obtain the intensities A_{in} (inside nanopores) and A_{out} (outside nanopores), as demonstrated in Figure 3.1. Since the total number of Na^+ cations (n_{tot}) associated with the entire NMR spectrum is known based on the amount of the injected electrolyte, the portion inside the P-40 nanopores could be calculated by

$$n_{\mathrm{in}} = n_{\mathrm{tot}} \frac{\mathrm{A_{in}}}{A_{\mathrm{in}} + A_{\mathrm{out}}} \tag{3.1}$$

Using the same procedure the amounts of water inside and outside nanopores can be determined. From these numbers the Na^+ concentration c inside the P-40 nanopores can be calculated. The concentrations of BF_4^- and NO_3^- inside and outside the nanopores can be determined similarly.

3.1.3 *In-situ* NMR on P-40 Supercapacitor

As a model system to investigate electrolyte properties under nanoconfinement, the electric conducting property of the activated carbons is an additional benefit which allows a fine control of the surface charge to tune the electrostatic interactions. This is achieved by incorporating a device similar to a supercapacitor [1-3] into the NMR probe. The modified supercapacitor design is shown in Figure 3.2. The supercapacitor consists of two electrodes made of pure P-40 separated by a glass fiber and immersed in the aqueous electrolyte (1 mol kg^{-1} $NaBF_4$ or $NaNO_3$). Each electrode is 3 mm long and 2.5 mm in diameter. One electrode is shielded with a copper foil so that the detected NMR signal comes only from a single electrode. Voltage is applied between the two electrodes. In the charging process, cations are driven away from the surface and anions are attracted to the surface on the positive electrode such that the net ionic charge on the electrolyte side balances the electric charge on the carbon surface.

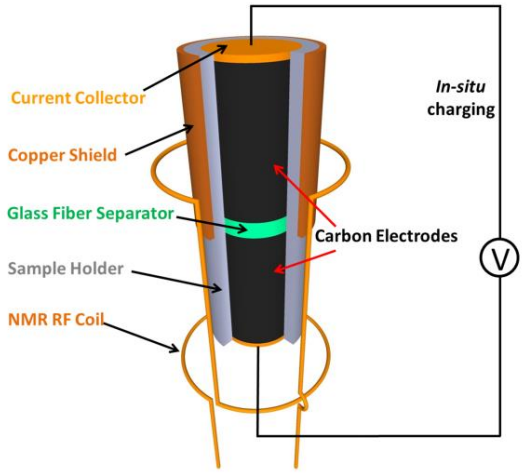

Figure 3.2: An illustration of the modified supercapacitor built into the NMR probe for controlling the P-40 surface charging. The device consists of two P-40 electrodes immersed in the electrolyte and separated by a glass fiber. One electrode is covered by a copper foil to enable a single-electrode NMR measurement which is carried out *in-situ* when voltage is applied between the two electrodes.

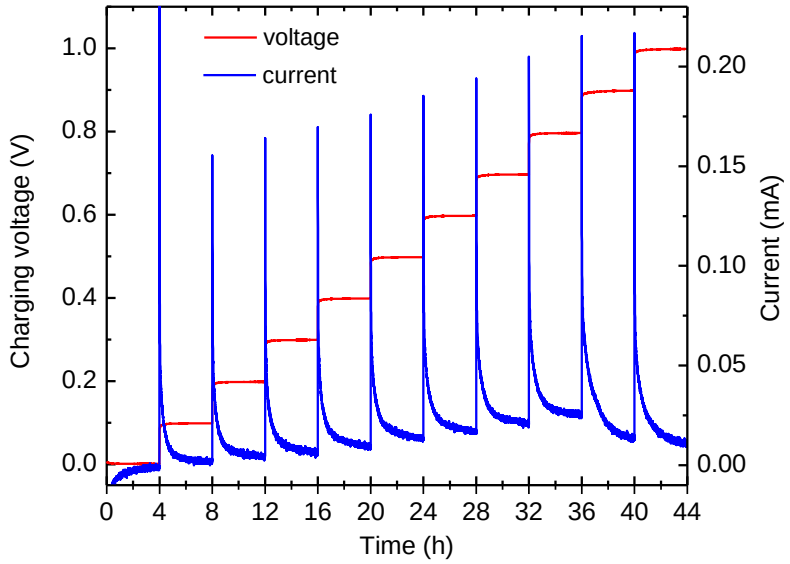

Figure 3.3: Plots of charging voltage vs. time and current vs. time. The voltage is increased by 0.1 V every 4 hours. A current spike is observed immediately after the voltage increase because of the capacitive charging. The charging process usually takes about 2 h because the device is not optimized for fast charging (no binder or carbon black is added to increase the conductivity and the electrode is very long). The electric current is not zero after 2 h probably due to the leaking current or some slow processes in the nanopores. Such slow processes are usually not useful for supercapacitors that undergo fast charging or discharging. So the spectrum taken after 3.5 h charging is used for analysis.

In-situ ^{19}F and ^{23}Na NMR experiments are carried out on a homemade probe which is equipped with a charging system controlled by Labview. The P-40 supercapacitor is charged from 0 V to 1.0 V with a step of 0.1 V. Figure 3.3 shows the typical curves of charging voltage vs. time and current vs. time. Each constant voltage step is held for 4 hours. A current spike is observed immediately after voltage is increased, indicating the capacitor charging. The current drops to a small value after about 2 hours, indicating equilibrium is reached. The small current is probably due to leakage or slow ionic processes in the ultromicropores. The static NMR spectra are acquired after 3.5 h charging for each step. For the ^{19}F NMR, the spin-lattice relaxation time (T_1) is 0.7 s and the last delay is 5 s. For ^{23}Na, T_1 is 20 ms and the last delay is 0.5 s. The charging has little effect on T_1, T_2^*, and the 90 degree pulses for both ^{19}F and ^{23}Na.

3.2 Results and Discussions

3.2.1 Electroneutrality Breakdown in Nanoconfinement

Figure 3.4 shows the normalized ion concentrations, c/c_0, where c is the average ion concentration in the nanopores and c_0 is the injected electrolyte concentration (1mol kg^{-1} except for NaF 0.8 mol kg^{-1} due to its lower water solubility), for NaF, $NaNO_3$, $NaBF_4$ electrolytes in P-40 and $NaBF_4$ electrolyte in P-92. One of the surprising phenomena revealed by measurements shown in Figure 3.4 is the drastic concentration difference between the cation and the anion, particularly significant in the nanoconfined aqueous electrolytes of $NaNO_3$ and $NaBF_4$. The concentration inside nanopores is c/c_0=1.92 for BF_4^- and c/c_0=0.64 for Na^+. In the larger pore sample of P-92, the ion concentration inside the nanopores is c/c_0=1.34 for BF_4^- and c/c_0=0.70 for Na^+. The anomalous concentration difference is a strong indication of the neutrality breakdown of the total charge inside the nanopores. As expected, the extent of electroneutrality

breakdown is less in P-92 which has larger pores. Nevertheless, the electroneutrality breakdown is still significant.

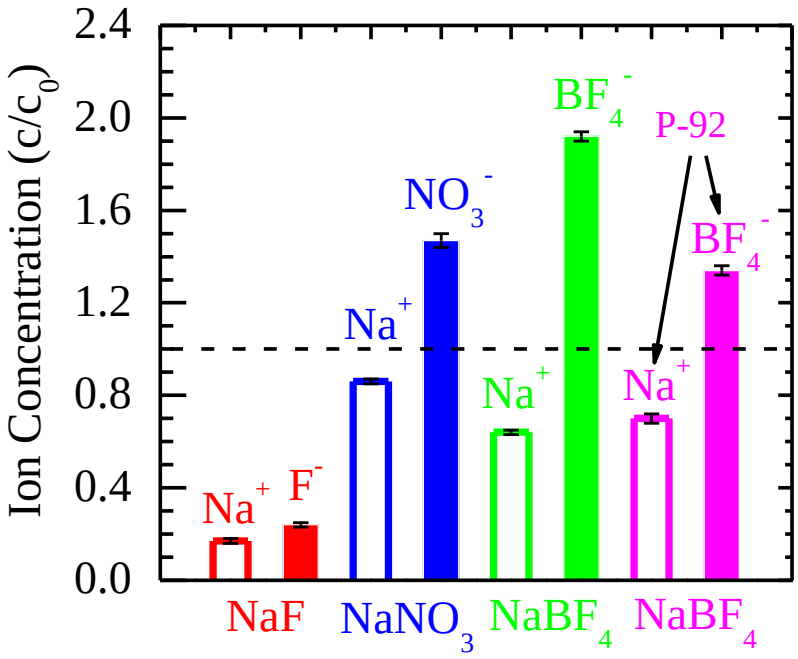

Figure 3.4: The cation and anion concentrations of NaF, $NaNO_3$, and $NaBF_4$ electrolytes inside the P-40 nanopores. The $NaBF_4$ electrolyte in a larger pore size sample (P-92) is also shown for comparison. The error bar is calculated using the error propagation method taking into account the standard error of the NMR spectrum deconvolution.

The possibility that the electrolyte neutrality might be maintained by other ions such as H^+, OH^- or the trace impurities can be ruled out in the current experimental approach. Take NaF electrolyte in P-40 as an example to estimate the amount of H^+ and OH^-. The PEEK-derived activated carbon is of high quality and has a low density of surface functional groups [4,5]. So all the H^+ and OH^- in this system are from water dissociation (depending on the point of zero charge and pH, the activated carbon can be positively or negatively charged, but the source of the charge still comes from water dissociation and the subsequent adsorption of H^+ or OH^-). Since only a limited electrolyte is injected into the activated carbon, the electrolyte amount in the

intergranular space is only about three times the amount inside the carbon nanopores. The intergranular electrolyte pH is measured to be 10 in the slurry. Therefore the net charge due to H^+ and OH^- inside the carbon nanopores is at most 3×10^{-4} mol kg^{-1}, which is negligible compared to the ion concentration inside the nanopores (Na^+ 0.17 mol kg^{-1}, F^- 0.24 mol kg^{-1}). Similar estimate can be applied to other ions and the trace impurities (less than 1%) in the as-purchased chemicals. Even if the impurities are all segregated into the nanopores, the maximum concentration is at most four times the impurity concentration in the bulk electrolyte. This would give rise to an estimated impurity concentration of 0.04 M, which is insignificant compared to the charge imbalance on the order of 0.5 M. This shows that the electroneutrality breakdown inside the carbon nanopores is an intrinsic property of the nanoconfined aqueous electrolytes in this system.

3.2.2 Specific Ion Effects on Ion Concentrations

Another intriguing phenomenon beyond the electroneutrality breakdown revealed by the data in Figure 3.4 is the strong influence of anions on the Na^+ concentration. Although the experiments are carried out with similar electrolyte concentrations and electrolyte/carbon ratios, the Na^+ concentrations vary significantly among different electrolytes. The Na^+ concentration for the NaF electrolyte in nanopores is highly suppressed while that for $NaNO_3$ is very close to the injected electrolyte concentration. It is interesting to note that the anion concentration increases in the order $F^- < NO_3^- < BF_4^-$ with F^- concentration being also highly suppressed in the nanopores while NO_3^- and BF_4^- concentrations being greatly enhanced. The $F^- < NO_3^- < BF_4^-$ ranking based on their concentrations is fully consistent with the ranking of the Hofmeister series where the anions are known to have different affinities toward a hydrophobic surface [6].

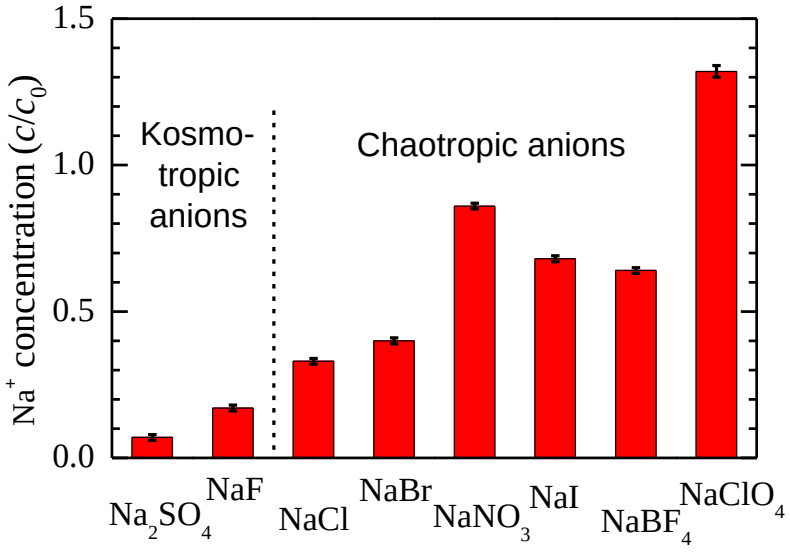

Figure 3.5: The Na^+ concentration inside nanopores for different sodium salt electrolytes plotted in the sequence of the Hofmeister series. The error bar is deduced using the same method described in Figure 3.4.

The systematic test on a series of sodium salt electrolytes, whose anions are chosen from the Hofmeister series $SO_4^{2-} < F^- < Cl^- < Br^- < NO_3^- < I^- < BF_4^- < ClO_4^-$, provides more insights into the anion-dependent Na^+ concentrations inside nanopores. The normalized average Na^+ cation concentration c/c_0 for the sodium salt series is shown in Figure 3.5. The Na^+ concentration in the nanopores increases gradually from Na_2SO_4 to $NaClO_4$ following the anion Hofmeister series with $NaNO_3$ being a clear exception (and slightly for NaI). It is of note that the Na^+ concentration in the nanopores is highly suppressed to $c/c_0<0.2$ for Na_2SO_4 and NaF, <0.4 for NaCl and NaBr, and <0.7 for NaI and $NaBF_4$. Even though I^- and BF_4^- are ranked to the right side (the chaotropic side) of NO_3^- in the Hofmeister series, c/c_0 =0.86 for $NaNO_3$ is significantly higher than that of NaI and $NaBF_4$. It is also of note that unlike other electrolytes, the Na^+ concentration in nanopores for $NaClO_4$ is substantially enhanced (c/c_0=1.32) compared to the bulk electrolyte concentration. Because a limited amount of electrolyte is added to the sample, the Na^+ concentration outside the nanopores also differs from c_0. The Na^+ concentration in

nanopores normalized by that outside the nanopores shows slightly different values from c/c_0. But the trend of the Na^+ concentration increase as well as the $NaNO_3$ anomaly remains the same.

The strongly anion-dependent Na^+ concentration inside the carbon nanopores revealed by the quantitative NMR analysis demonstrates the intriguing interplay between cations and anions. Na^+ is a strongly hydrated cation with a hydration free energy of -87 kcal/mol, hydration number of 5 to 6 in the first hydration shell [7,8], and no affinity toward a hydrophobic surface [9]. In fact, the strong hydration leads to a free energy barrier of several k_BT (T=300 K) or higher for Na^+ ions to enter a hydrophobic nanopore with the diameter less than 2 nm [10]. This is clearly reflected by the low value of c/c_0<0.2 for Na^+ in NaF. Theories predict $F^- < Cl^- < I^-$ to be the ranking based on their affinity toward a hydrophobic surface [9]. This trend is expected to hold for most anions in the Hofmeister series where the hydration enthalpy becomes less negative toward the chaotropic side of the series [11]. In the nanopore confinement, the different ion-water and ion-surface interactions among those anions lead to the difference in the Na^+ cation concentration.

The specific ion effects are ubiquitous in electrochemical and biological systems [6,9,12,13]. It is fascinating that the ions' effects on many different properties such as viscosity [14,15] and surface tension [21,33] all follow the same trend as described by the Hofmeister series. The commonality here is the ion hydration and the unique properties of water. It was suggested [6] that the Jones-Dole coefficient B in viscosity is positive (e.g., F^-) when the ion-water interaction is stronger than the water-water interaction, whereas it is negative when the water-water interaction is stronger than the ion-water interaction (e.g., BF_4^- and NO_3^-). In fact, the sign change in B (positive to negative) is correlated with the NMR observation that the anion concentration changes from being suppressed to being enhanced. This indicates that the relative

strength of the ion-water interaction versus the water-water interaction also plays a dominant role in the specific ion effects in nanoconfinement.

3.2.3 Ion Distribution Theory

More insight into the anion's influence on the Na^+ concentration can be gained by looking at the various factors determining the ion distribution near the interface. The ion distribution for ion *i* with valency z_i is given by [16,17]

$$\rho_i(x) = \frac{\exp\left(\frac{\mu_i}{k_B T}\right)}{\Lambda_i^3} \exp\left(-\frac{z_i e\psi(x) + V_i^{ext}(x) + corr_i(x)}{k_B T}\right) \quad (3.2)$$

where *e* is the elementary charge, Λ_i is the de Broglie thermal wavelength of ion *i*, μ_i is the chemical potential of ion *i*, $\psi(x)$ is the electrostatic potential at the location *x* inside the nanopores, $V_i^{ext}(x)$ is the ion-surface potential that depends on the ion-specific affinity toward the interface [17,18], and $corr_i(x)$ is the free energy contribution from ion-ion correlations. For 1 mol L^{-1} monovalent ions, the electrostatic correlation [19] is of minor importance and $corr_i(x)$ is dominated by excluded-volume interactions. $corr_i(x)$ can be obtained from theories or molecular dynamics simulations [17] that include molecular-scale structural information. In general, $corr_i(x)$ depends on both the ion-specific short-ranged pair potential and the ion concentrations. The latter are implicitly affected by the electrostatic potential $\psi(x)$. The ion concentration measured by NMR is the value averaged over the pore width *d*:

$$\bar{\rho}_i = \frac{1}{d}\int_0^d \rho_i(x)dx \quad (3.3)$$

Although the ion-surface potential $V_i^{ext}(x)$ depends on the distance between the ion and the surface [18,20], it is expected that the mean potential $\bar{V}_i^{ext}$ for anions in P-40 nanopores, defined by

$$\exp(-\beta\bar{V}_i^{ext}) = \frac{1}{d}\int_0^d \exp(-\beta V_i^{ext}(x))dx \quad (3.4)$$

follows the anion ranking in the Hofmeister series. As such, a larger $-\bar{V}_i^{\text{ext}}$ value for the more chaotropic anion would lead to a higher anion concentration in the nanopores and that would attract more Na^+ counterions electrostatically. Of course, this argument does not take into considerations of the ion-ion correlations (i.e. $corr_i(x) = 0$).

In electrolytes, ions don't just interact with the mean electrostatic field. They are also affected by the neighboring ions through short-ranged pair interactions, that is, the ion-ion correlations. These interactions also contribute to the total free energy and have an impact on the ion distribution. The ion-ion correlations can have electrostatic origins. For instance, if there is a cation at position ***r***, there will be a reduced probability to find another cation and an enhanced probability to find an anion in its vicinity because of the Coulomb interactions. The ion-ion correlations can also have nonelectrostatic origins. For instance, ions cannot occupy the same position because of their finite ion size. This leads to the excluded-volume correlation [20,21]. In addition, an attractive or repulsive potential can also be resulted from the ion hydration and the water-mediated interactions [17,20]. The ion-ion correlations based on the electrostatic and ion-specific interactions are predicted to be of crucial importance in nanoconfined electrolytes [17,19,22,23]. Although the preferentially adsorbed anions in the nanopores could attract Na^+ cations via electrostatic interactions as demonstrated by the experiments, the higher Na^+ concentration associated with the $NaNO_3$ electrolyte is not due to the anomalous interfacial affinity of NO_3^-, since its concentration is consistent with the ranking of the Hofmeister series, i.e. lower than the BF_4^- concentration (Figure 3.4). Clearly, the ion-ion correlations must be invoked to explain the abnormal Na^+ concentration in $NaNO_3$. The correlations of Na^+ with NO_3^- appear to be stronger than that with I^- and BF_4^-, suggesting a more negative mean correlation ($\overline{corr}_+$) for Na^+ inside the nanopores, defined by

$$\exp(-\beta\overline{corr}_{+}) = \frac{1}{d}\int_0^d \exp(-\beta corr_{+}(x))dx \quad (3.5)$$

It is interesting to note that the formation of solvent-separated Na^+ and NO_3^- ion pairs in the bulk electrolyte has been recognized by both computational and experimental studies [24,25]. The formation of solvent-separated Na^+ and ClO_4^- ion pairs was also found in the bulk electrolyte [26]. Such molecular-scale ion-ion correlations could become more significant at the interface and in the nanoconfined environment, giving rise to the observed anomaly in the Na^+ concentration of $NaNO_3$ and the substantially enhanced Na^+ concentration in the $NaClO_4$ aqueous electrolyte.

3.2.4 Ion Concentrations in Charged Nanopores

To demonstrate how the nonelectrostatic specific ion effects, including the ion-ion correlations, dominate the electrostatic interactions inside the nanopores and lead to the intriguing electroneutrality breakdown, the dependence of the ion concentration on the confining wall surface charging is measured with the *in-situ* NMR [27-29]. Figure 3.6 shows the ion concentration inside P-40 nanopores versus the charging voltage for $NaBF_4$ electrolyte. The anions and cations are measured by ^{19}F and ^{23}Na NMR respectively. With positive charging (+V), both the Na^+ and BF_4^- concentrations respond linearly to the charging voltage. The influence of the nonelectrostatic interactions is reflected on the huge initial concentration difference at 0 V. Because the surface is already crowded with anions at 0 V, further positive charging is unlikely to bring in more anions to the surface where the nonelectrostatic interaction dominates. Therefore, such a linear behavior is expected because the ion concentration change is mainly due to the ions away from the interface and is affected by the change of the electrostatic interaction.

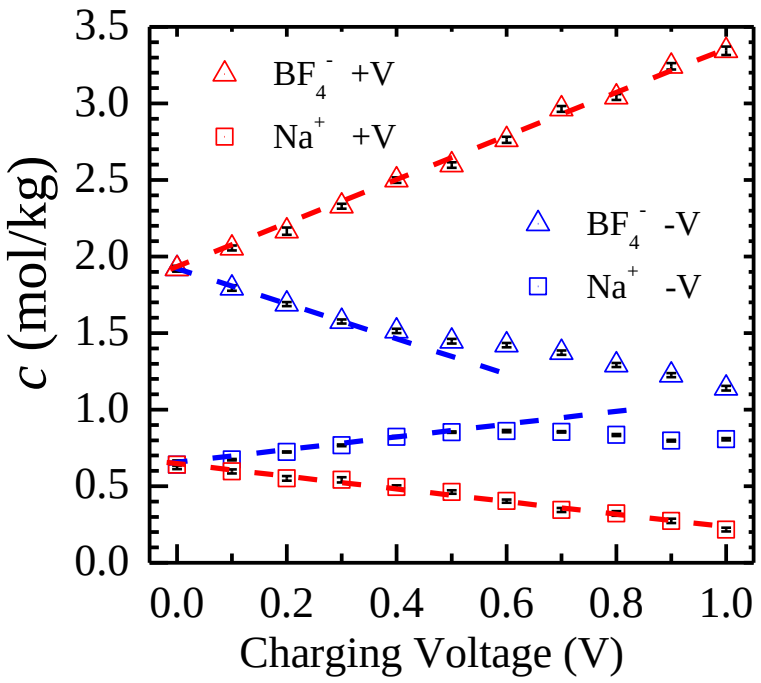

Figure 3.6: Nanoconfined ion concentrations for 1 mol kg^{-1} $NaBF_4$ electrolyte in P-40 versus the charging voltage. The error bars are calculated from the standard error of the NMR spectrum peak fitting.

In contrast, both Na^+ and BF_4^- exhibit nonlinear behaviors with negative charging (-V). The Na^+ concentration increases with voltage from 0 to 0.6 V but then starts to decrease with further negative charging. Concomitantly, the initial linear decrease of the BF_4^- concentration levels off beyond 0.6 V. The nonlinear behavior, particularly the unexpected Na^+ concentration decrease with negative charging beyond 0.6 V, demonstrates the competing effect between the ion-ion correlations and the ion-surface electrostatic interactions. The attractive Coulomb interaction between Na^+ and the negatively charged surface tends to bring Na^+ into the nanopores, whereas the decreased BF_4^- concentration favors dragging Na^+ out of the nanopores. When the latter effect dominates, the Na^+ concentration can actually decrease with further negative charging. It is also interesting to note that even at 1.0 V charging, the BF_4^- concentration in the nanopores is still higher than that of Na^+, demonstrating the strong ion-surface attractions that

overcomes the enormous Coulomb forces due to the net charge in the nanopores and the repulsion between the anions and the negative charged surface.

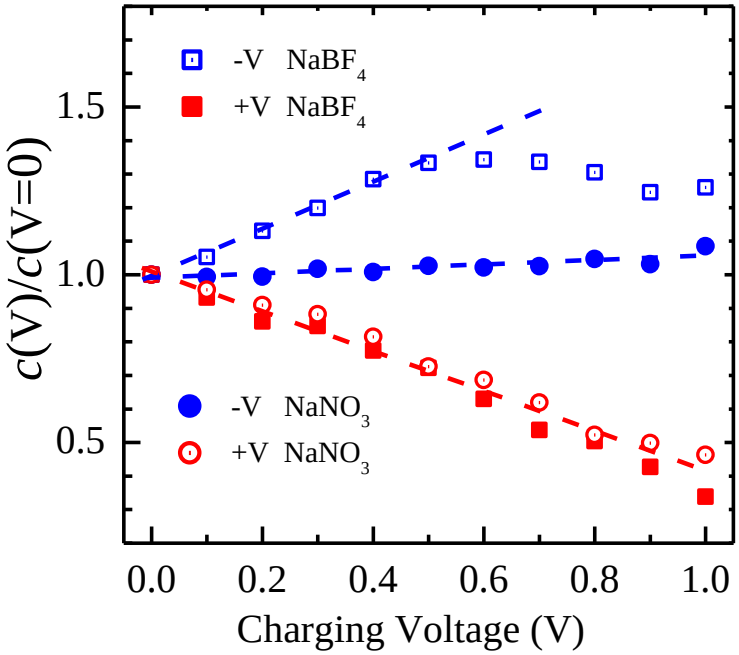

Figure 3.7: Comparison of the Na^+ concentrations $c(V)/c(0)$ for $NaBF_4$ and $NaNO_3$ electrolytes versus the charging voltage. The error bars are smaller than the marker size.

The influence of anions on the cation's behavior via the ion-ion correlations is evidenced by comparing the Na^+ behaviors for $NaBF_4$ and $NaNO_3$ electrolytes shown in Figure 3.7. For the convenience of comparison, the concentration has been normalized by their respective value at 0 V. With positive charging, the Na^+ concentration in both $NaBF_4$ and $NaNO_3$ decreases linearly because it is mainly affected by the change in electrostatic interactions. However, drastically different behaviors are observed with negative charging: while the Na^+ concentration in $NaBF_4$ electrolyte first increases then decreases, the Na^+ concentration for $NaNO_3$ changes much less with charging voltage, indicating that the correlation between Na^+ and NO_3^- is stronger than that in $NaBF_4$. The Coulomb attraction between the cations and the negatively charged surface is

completely compensated by the ion-ion correlations which drag Na^+ out of the nanopores when the anions are repelled from the nanopores.

3.3 Conclusions

In summary, a quantitative NMR measurement was employed to investigate the electroneutrality condition in nanoconfined aqueous electrolytes. A substantial electroneutrality breakdown of the total charge was observed inside uncharged activated carbon nanopores. The ion-specific interfacial interactions and the ion-ion correlations were found to play critical roles in determining the extent of the electroneutrality breakdown. These effects were further investigated in charged carbon nanopores which led to strong asymmetric responses between cations and anions to the confining wall surface charging. Moreover, the anion imposes a great influence on the cation's behavior via the ion-ion correlations.

This study demonstrates that graphite-like porous carbon provides an ideal model system and the novel *in-situ* NMR approach opens a new avenue for quantitative experimental evaluations of various ion-specific interactions near the interface and under nanoconfinement. Although our work is based on aqueous electrolytes, it can be generally applied to other systems such as organic electrolytes and ionic liquids, where the strong ion-specific properties beyond the electrostatic interactions (e.g. ion solvation, interaction with the surface, ion-ion correlations) are also of relevance. The NMR approach is also of great value for comparing theoretical models [20,30,31], where the possibility of the nanoconfinement-induced electrolyte non-neutrality is often ignored and the neutrality of the total charge in nanoconfined regions is usually assumed *a priori*.

3.4 REFERENCES

1. Conway, B., *Electrochemical supercapacitors: scientific fundamentals and technological applications*. (Kluwer Academic/Plenum. New York, 1999).

2. Chmiola, J., Yushin, G., *et al. Science* **313**, 1760-1763 (2006).

3. Zhu, Y., Murali, S., *et al. Science* **332**, 1537-1541 (2011).

4. Wang, H.-J., Kleinhammes, A., *et al. J. Phys. Chem. C* **118**, 8474–8480 (2014).

5. Cansado, I. P., Gonçalves, F., *et al. Fuel Process. Technol.* **90**, 232-236 (2009).

6. Kunz, W., *Specific ion effects*. (World Scientific, Singapore, 2010).

7. Marcus, Y. *Biophys. Chem.* **51**, 111-127 (1994).

8. Rempe, S. B. and Pratt, L. R. *Fluid Phase Equilib.* **183**, 121-132 (2001).

9. Jungwirth, P. and Tobias, D. J. *Chem. Rev.* **106**, 1259-1281 (2006).

10. Beckstein, O., Tai, K., *et al. J. Am. Chem. Soc.* **126**, 14694-14695 (2004).

11. Smith, D. W. *J. Chem. Educ.* **54**, 540 (1977).

12. Lo Nostro, P. and Ninham, B. W. *Chem. Rev.* **112**, 2286-2322 (2012).

13. Zhang, Y. and Cremer, P. S. *Curr. Opin. Chem. Biol.* **10**, 658-663 (2006).

14. Jenkins, H. D. B. and Marcus, Y. *Chem. Rev.* **95**, 2695-2724 (1995).

15. Collins, K. D. *Methods* **34**, 300-311 (2004).

16. Hansen, J.-P. and McDonald, I. R., *Theory of simple liquids: with applications to soft matter*. (Academic Press, 2013).

17. Kalcher, I., Schulz, J. C., *et al. J. Chem. Phys.* **133**, 164511 (2010).

18. Horinek, D. and Netz, R. R. *Phys. Rev. Lett.* **99**, 226104 (2007).

19. Levin, Y. *Rep. Prog. Phys.* **65**, 1577 (2002).

20. Kalcher, I., Schulz, J. C., *et al. Phys. Rev. Lett.* **104**, 097802 (2010).

21. Messina, R., González-Tovar, E., *et al. EPL (Europhysics Letters)* **60**, 383 (2002).

22. Buyukdagli, S. and Ala-Nissila, T. *J. Chem. Phys.* **140**, 064701 (2014).

23. Laanait, N., Mihaylov, M., *et al. Proc. Natl. Acad. Sci. U.S.A.* **109**, 20326-20331 (2012).

24. Yu, J.-Y., Zhang, Y., *et al. J. Phys. Chem. B* **116**, 12581-12589 (2012).

25. Riddell, J., Lockwood, D., *et al. Can. J. Chem.* **50**, 2951-2962 (1972).

26. Miller, A. G. and Macklin, J. W. *J. Phys. Chem.* **89**, 1193-1201 (1985).

27. Forse, A. C., Griffin, J. M., *et al. PCCP* (2013).

28. Wang, H., Köster, T. K. J., *et al. J. Am. Chem. Soc.* **133**, 19270-19273 (2011).

29. Wang, H., Forse, A. C., *et al. J. Am. Chem. Soc.* **135**, 18968-18980 (2013).

30. Argyris, D., Cole, D. R., *et al. ACS Nano* **4**, 2035-2042 (2010).

31. Kalluri, R. K., Konatham, D., *et al. J. Phys. Chem. C* **115**, 13786-13795 (2011).

CHAPTER 4 NUMERICAL CALCULATION OF ION DISTRIBUTION IN SLIT NANOPORE

In the previous chapter, the NMR experiment reveals the electroneutrality breakdown inside carbon nanopores and how it varies with the pore size and the ion properties. Here I propose a new model to solve the generalized PB equation in slit-shaped nanopores. The numerical calculation supports the conclusion that the electroneutrality breakdown is caused by the ion-specific interfacial interactions and the ion-ion correlations.

4.1 Introduction

The PB equation is widely used to predict the interfacial ion distribution and the double-layer force in electrochemistry, colloidal science, biological and geological physics [1-3]. Several assumptions are made to solve the PB equation to obtain the electrostatic potential in the diffuse layer. For example, ions are treated as point charges and the finite ion size is ignored, they only interact with the mean electrostatic field and the nonelectrostatic interactions (such as the hydration shell overlapping in high concentrations) are not accounted for, the solvent is assumed to be a continuum with a constant permittivity, etc. Because of these limitations, the PB equation is only appropriate for the situation of low salt concentrations (smaller than 0.2 M for a monovalent electrolyte) and for potentials not exceeding 50-80 mV. Significant improvements have been made in the last two decades [4-11] in the quantitative prediction of the double layer capacitance even for room temperature ionic liquids (RTIL). The finite ion size and the excluded volume are taken into account [4,10,11]. The effect of ion polarizability and image charge are

considered [5-7,9,10,12]. The short-ranged electrostatic and nonelectrostatic correlations beyond the mean field interactions are also addressed [8,11,13-15].

On a planar surface, the surface charge density is commonly used as a boundary condition to solve the PB equation [16]. The surface charge usually results from ion adsorption to the surface or ionization of the surface functional groups. A zero net charge is assumed if there is no specific ion adsorption and no functional groups, as in the case of the water/air interface [7,12] or the self-assembled monolayer (SAM)-water interface [6]. While this boundary condition works well on electrochemical surfaces without nanoconfinement or in large nanochannels, it could not predict the observed electrolyte non-neutrality in uncharged carbon nanopores. A possible reason is that induced surface charge is not accounted for in the boundary condition. Considering the increasing interest in the application of nanoelectrochemistry [17,18], supercapacitors [19-25] and nanofluidics [26-28], it is worthwhile to look for solutions based on new models that do not require this boundary condition.

4.2 Theoretical Development

4.2.1 Nanopore Model

The nanopore model is shown in Figure 4.1. Two large perfect conductor plates (infinite electric conductivity) are separated by a distance d to provide the 1D planar nanopore confinement. The conductor plate assumption is to simplify the calculation but the methodology can be generally applied to thin (nanometer thickness) and non-conducting confining materials. The pore center is located at x=0. The nanopore wall (the inner surface of the plate) is located at x_1 and the outer surface (toward the bulk solution side) is located at x_2. Since a perfect conductor is assumed, the thickness of the plate does not matter as all charges will be screened by the plate. The ion has a radius a, which defines the closest distance from the ion center to the surface, i.e.

the Helmholtz plane. I assume initially that cations and anions have the same radius, and later discuss different ion radii (a_+ and a_-). A monovalent aqueous electrolyte with a concentration of 1 mol/L is used. The solvent water is treated as a continuum with dielectric constant $\varepsilon = 78.5$. At room temperature (298K), the Debye length is 0.304 nm.

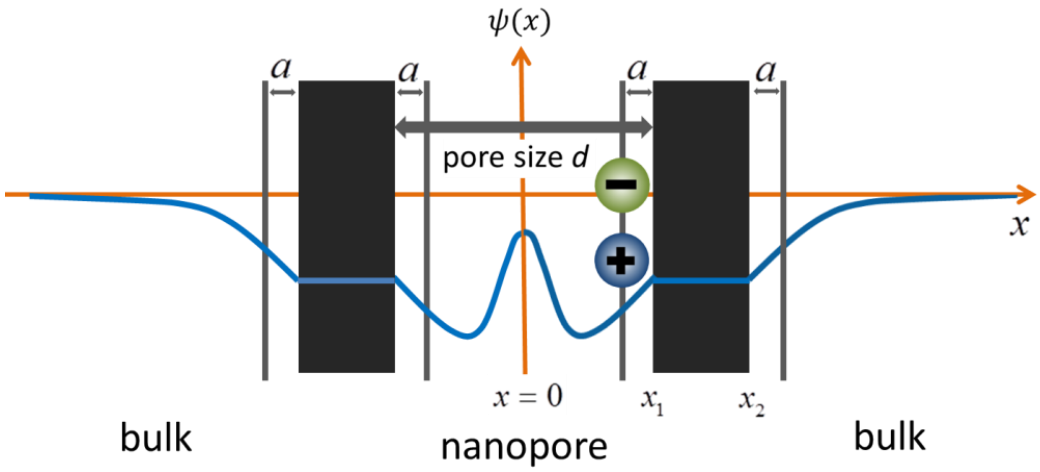

Figure 4.1: The 1D slit-shaped nanopore model. The electrodes are treated as two large perfect conductors. The pore center is located at x=0. The inner surface of the plate is located at x_1 and the outer surface is located at x_2. a is the ion radius which defines the closest distance from ion center to the surface. The blue curve is an illustrative electric potential distribution.

4.2.2 Generalized PB Equation

The Poisson's equation in electrostatics relates the electric potential ψ to the excess charge density ρ,

$$\nabla^2\psi = -\frac{\rho}{\varepsilon\varepsilon_0} \tag{4.1}$$

where ε is the dielectric constant and ε_0 is the vacuum permittivity. The charge density ρ is determined by both the concentrations of cations and anions,

$$\rho = z_+c_+F + z_-c_-F \tag{4.2}$$

here z_i and c_i are the valency and the concentration of the ions, respectively. *F* is the Faraday constant. For symmetric monovalent electrolytes, $z_+ = 1$ and $z_- = -1$. The ion concentration is described by the Boltzmann distribution,

$$c_i = c_0 \exp(-\frac{z_i e\psi + V_i + corr_i}{k_B T}) \tag{4.3}$$

where c_0 is the ion concentration of the bulk solution and it is the same for both the cations and anions. $z_i e\psi + V_i + corr_i$ is the energy of ion *i* relative to the bulk phase. It consists of three contributions: the electrostatic potential energy $z_i e\psi$, potential of the mean force for the ion-surface interactions V_i, and the free energy contribution from the ion-ion correlations $corr_i$. k_B is the Boltzmann constant and *T* is temperature. Combining Eq. (4.1) - Eq. (4.3) leads to the generalized PB equation,

$$\nabla^2 \psi = -\sum_i \frac{z_i c_0 F}{\varepsilon \varepsilon_0} \exp(-\frac{z_i e\psi + V_i + corr_i}{k_B T}) \tag{4.4}$$

In the 1D planar nanopore model, ψ, V_i and $corr_i$ only depends on *x*, so Eq. (4.4) reduces to

$$\frac{d^2\psi(x)}{dx^2} = -\sum_i \frac{z_i c_0 F}{\varepsilon \varepsilon_0} \exp(-\frac{z_i e\psi(x) + V_i(x) + corr_i(x)}{k_B T}) \tag{4.5}$$

If only the electrostatic interactions are accounted for, Eq. (4.5) is further simplified as

$$\frac{d^2\psi(x)}{dx^2} = \frac{2c_0 F}{\varepsilon \varepsilon_0} \sinh(\frac{e\psi(x)}{k_B T}) \tag{4.6}$$

Setting $y(x) = \frac{e\psi(x)}{k_B T}$ and $\kappa = \sqrt{\frac{2ec_0 F}{\varepsilon \varepsilon_0 k_B T}}$ ($\frac{1}{\kappa}$ is called Debye length λ_D) leads to the PB equation which has been widely used to describe the electric double layer.

$$\frac{d^2 y}{dx^2} = \kappa^2 \sinh(y) \tag{4.7}$$

4.2.3 Ion-Surface Interactions

The potential of mean force for the ion-surface interactions V_i in Eq. (4.5) could be modeled in several different ways. Realistic potentials could be obtained via MD simulations [29,30] where the ion is fixed near the interface and the position-dependent mean force is calculated. A potential is obtained by integrating the mean force. Because the ion-surface potential [6,29] and the ion-ion correlation [11,30,31] from MD simulations are not available for the system investigated here, the ion-ion correlation is not considered at this moment and a simplified ion-surface potential [5] is used in this chapter,

$$V_i(x) = \frac{B_i}{x^3} \tag{4.8}$$

Here x is the distance between the ion center and the surface; B_i characterizes the strength of the ion-specific interactions with the surface and its value is about a few $k_B T$ near the surface [32]. The inverse cubic dependence comes from the dipole-dipole interaction between the ion and its image charge. A negative B_i indicates an attractive interaction with the surface and a positive B_i indicates a repulsive interaction. The finite ion radius guarantees that the potential in Eq. (4.8) does not diverge. To focus on the effects of the ion-specific nonelectrostatic interactions, the electrostatic interaction with its image charge is not accounted here since it is not ion-specific.

Inside the nanopores, ions have interactions with the surfaces on both sides, therefore

$$V_i(x) = \frac{B_i}{(\frac{d}{2} + x)^3} + \frac{B_i}{(\frac{d}{2} - x)^3} \tag{4.10}$$

Here $\frac{d}{2} + x$ and $\frac{d}{2} - x$ are the distances to the left inner wall and the right inner wall respectively. In the bulk solution near the outer surface, ions only interact with one surface, so

$$V_i(x) = \frac{B_i}{(x - x_2)^3} \tag{4.11}$$

$x - x_2$ is the distance from the ion in the bulk solution to the plate outer surface.

Since $corr_i(x) \equiv 0$ is assumed at this moment, the following generalized PB equation is to be discussed throughout this chapter with $V_i(x)$ defined by Eq. (4.10) and Eq. (4.11):

$$\frac{d^2\psi(x)}{dx^2} = -\sum_i \frac{z_i c_0 F}{\varepsilon\varepsilon_0} \exp(-\frac{z_i e\psi(x) + V_i(x)}{k_B T}) \tag{4.12}$$

4.2.4 Boundary Conditions

The boundary conditions are crucial to the solution of the generalized PB equation. In the conventional treatment, the surface charge density on the confining wall is usually assumed and the PB equation is solved only inside the nanopores. The total ionic charge from the electrolyte in the nanopores completely balances the total charge on the wall [27,33]. If the confining wall is initially uncharged, a zero surface charge density is then assumed. This assumption is not necessary true as it will be shown later that induced charge is possible on the plate surface. In contrast to the conventional method, in this chapter the PB equation is solved jointly for both regions inside and outside the nanopore (joint model). This approach does not require a known surface charge density *a priori*.

Since the system is symmetric about the y axis, we only need to solve the positive *x* part. The solution is divided into two pieces (inside and outside the nanopore) which are linked by appropriate boundary conditions. Because Eq. (4.12) is a second order ordinary differential equation, the two pieces require four boundary conditions to ensure a unique solution.

The first boundary condition is

$$\left.\frac{d\psi}{dx}\right|_{x=0} = 0 \tag{4.13}$$

that is, the potential at x=0 is a local maximum or minimum, because the model is symmetric about $x = 0$.

The second boundary condition is

$$\psi\big|_{x=\infty} = 0 \tag{4.14}$$

because the bulk solution is neutral.

The solutions to the generalized PB equation in the two regions are not independent. The relationship in the electric potential and the total charge between the two regions determines the other two boundary conditions. The net charge on the plate is zero, meaning the total charge in the bulk solution side should compensate the total charge inside the nanopore so that the overall system is electroneutral. The total charge density per surface area in the nanopore region $0 < x < \frac{d}{2} - a$ is

$$\sigma_{in} = \int_0^{\frac{d}{2}-a} \rho(x)dx = \int_0^{\frac{d}{2}-a} -\varepsilon\varepsilon_0 \frac{d^2\psi}{dx^2} dx = \varepsilon\varepsilon_0 \left(\frac{d\psi}{dx}\Big|_{x=0} - \frac{d\psi}{dx}\Big|_{x=\frac{d}{2}-a}\right) = -\varepsilon\varepsilon_0 \frac{d\psi}{dx}\Big|_{x=\frac{d}{2}-a} \tag{4.15}$$

here $\frac{d\psi}{dx}\Big|_{x=0} = 0$ is used according to the boundary condition in Eq. (4.13). The total charge density per surface area in the region outside the nanopore ($x > x_2 + a$) is

$$\sigma_{out} = \int_{x_2+a}^{\infty} \rho(x)dx = \int_{x_2+a}^{\infty} -\varepsilon\varepsilon_0 \frac{d^2\psi}{dx^2} dx = \varepsilon\varepsilon_0 \left(\frac{d\psi}{dx}\Big|_{x=x_2+a} - \frac{d\psi}{dx}\Big|_{x=\infty}\right) = \varepsilon\varepsilon_0 \frac{d\psi}{dx}\Big|_{x=x_2+a} \tag{4.16}$$

Here the condition $\frac{d\psi}{dx}\Big|_{x=\infty} = 0$ is assumed since it is in the bulk solution. Since the conductor plate carries no net charge (to mimic the initially non-charged carbon), the electroneutrality condition on the whole system requires

$$\sigma_{in} + \sigma_{out} = \int_0^{\frac{d}{2}-a} \rho(x)dx + \int_{x_2+a}^{\infty} \rho(x)dx = 0 \quad \Rightarrow \quad \frac{d\psi}{dx}\Big|_{x=x_2+a} - \frac{d\psi}{dx}\Big|_{x=\frac{d}{2}-a} = 0 \tag{4.17}$$

This is the third boundary condition.

The physical picture behind Eq. (4.17) is that electric charge is induced on the inner surface and the outer surface. Because perfect conductor plates are assumed, the net charge inside the nanopore is completely screened by the induced charge on the inner surface of the conductor plate. So is the net charge on the bulk solution side. The induced charge on the inner surface and outer surface has the same amount but different signs.

In the regions close to the surface, i.e. $\frac{d}{2} - a < x < \frac{d}{2}$ and $x_2 < x < x_2 + a$, the electric potential changes linearly due to the absence of the ionic charge, resembling the situation in a parallel plate capacitor. The capacitance per surface area, often referred to as the Helmholtz capacitance in the double layer theory [34,35], is

$$C_H = \frac{\varepsilon\varepsilon_0}{a} \tag{4.18}$$

The capacitance value varies if different dielectric constant ε is used. For example, ε for interfacial water is much different from the bulk water because of the dipole saturation in the EDL [36,37]. Other factors such as the image charge can also modify the capacitance [9], leading to a result different from Eq. (4.18).

The potential drop between the inner surface located at x_1 and the Helmholtz plane located at $\frac{d}{2} - a$ is

$$\psi(\frac{d}{2} - a) - \psi(x_1) = \frac{\sigma_{in}}{C_H} \tag{4.19}$$

Similarly, the potential drop between the outer surface located at x_2 and the Helmholtz plane located at $x_2 + a$ is

$$\psi(x_2 + a) - \psi(x_2) = \frac{\sigma_{out}}{C_H} \tag{4.20}$$

Because the conductor is an equal-potential body, $\psi(x_1) = \psi(x_2)$ and $\sigma_{in} = -\sigma_{out}$, combining Eq. (4.19) and Eq. (4.20) gives rise to the forth boundary condition

$$\psi(x_2 + a) - \psi(\frac{d}{2} - a) = \frac{2\sigma_{out}}{C_H} = \frac{2\varepsilon\varepsilon_0}{C_H} \frac{d\psi}{dx}\Big|_{x=x_2+a} \tag{4. 21}$$

With the four boundary conditions, i.e. Eq. (4.13), (4.14), (4.17) and (4.21), a unique solution of the generalized PB equation can be obtained for the whole space $0 < x < \infty$, including both the regions inside and outside the nanopore. The surface potential and the induced surface charge density on the plate can be determined as well after the solution is found.

4.3 Results

4.3.1 Ion Distribution in 1 nm Slit-Shaped Pores

The generalized PB equation is solved for typical parameters $a = 0.35\,\text{nm}$, $B_- = -58 \times 10^{-50}$ Jm^3, $B_+ = 46 \times 10^{-50}$ Jm^3 and $C_H = 400\,\mu\text{F/cm}^2$ in the 1 nm pore (d=1 nm). 0.35 nm is the typical radii for hydrated ions [2]. The chosen ion-surface potential corresponds to an adsorption energy of about $5\,k_B T$ at 0.3 nm from the surface, which is in line with the MD simulation results [6]. The Helmholtz capacitance C_H is 200 μF/cm^2 according to Eq. (4.17) if the bulk water dielectric constant 78.5 is used. Here a much larger value for C_H is used because the image charge contribution on the metal/liquid interface could significantly increase the capacitance [9].

The ion distribution in the 1nm pore is shown in Figure 4.2. Near the surface, anions are preferentially adsorbed while cations are repelled. This is because an attractive potential is chosen for anions and a repulsive potential for cations. Although the anion concentration decreases as the position moves toward the pore center, it is still higher than the bulk concentration (1mol/L) because the attractive potential extends throughout the whole pore region. The cation concentration increases as the location moves away from the surface and exceeds the bulk concentration in the pore center but it is still smaller than the anion's. The average ion concentration inside the nanopore is 2.44 mol/L and 0.84 mol/L for anions and cations, respectively, indicating an electroneutrality breakdown of the total nanoconfined charge.

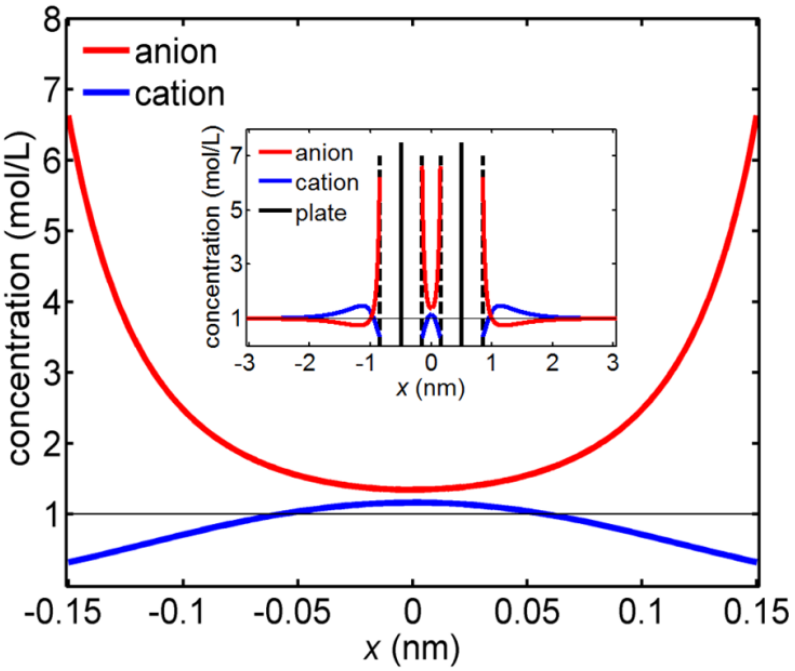

Figure 4.2: Ion distribution in the 1 nm pore for parameters $B_+ = 46\times10^{-50}$ J m^3, $B_- = -58\times10^{-50}$ J m^3. The inset includes the ion distributions both inside and outside the nanopore. The vertical solid lines are the infinitely thin conducting plates and the vertical dashed lines are the Helmholtz planes. There is no ion distribution between the Helmholtz plane and the conducting plate because the ion has a finite size and can't get to the surface too close.

The inset in Figure 4.2 shows the ion concentrations both inside and outside the nanopore. Distinctive behaviors are observed between the two regions. Although anions accumulate near the outer surface and cations are repelled, the spacious room in the bulk solution permits a region where the cation concentration is much higher than the anion's. This region can extend more than 1 nm away from the surface. The net charge in the bulk solution is positive and balances the net negative charge inside the nanopore to satisfy the total charge neutrality condition.

4.3.2 Electrostatic and Nonelectrostatic Potential Energies

The ion distributions are determined by the interplay between electrostatic interactions and the ion-surface potentials (ion-ion correlations not considered here) as described by Eq. (4.3). More insights on the interfacial behaviors can be gained by comparing the various interactions. Figure 4.3 shows the distributions of $V_+(x)$, $V_-(x)$ and the electrostatic potential. The magnitude is plotted here for the convenience of comparison. The electrostatic potential energy stays fairly constant (about 2 $k_B T$) inside the nanopore, but $V_+(x)$ and $V_-(x)$ decreases sharply as the position moves away from the surface. As a result, the energy is dominated by the short-range ion-surface potentials near the surface, no matter whether it is inside or outside the nanopore. Despite the higher ion-surface potentials inside the nanopores (compared with those outside at the same distance from the surface) due to the superposition of interactions from both the surfaces, the total energy near the inner surface in fact is very similar to the total energy near the outer surface, as shown in the inset of Figure 4.3. This is because the electrostatic potential is also lower on the outer surface. Figure 4.3 also reveals an important distinction between the nanopore and the bulk region. Due to the limited space in the nanopore, the ion-surface potentials do not drop blow the electrostatic potential significantly while they do in the bulk solution. As a consequence, a region

(between 1 nm and 2 nm) dominated by the electrostatic potential is observed near the outer surface.

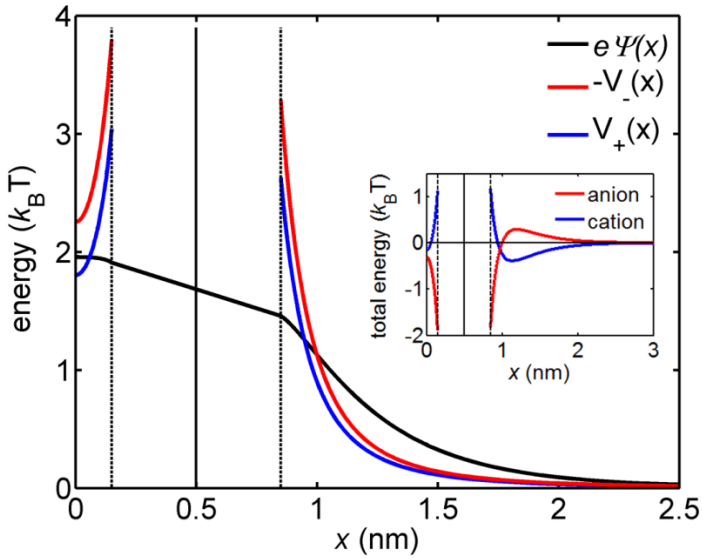

Figure 4.3: Comparing the distribution of ion-surface potentials $V_+(x)$, $V_-(x)$ and the electrostatic potential. The negative half space is not shown since the pore is symmetric. The magnitude of $V_+(x)$ and $V_-(x)$ is plotted for the convenience of comparison. The actual $V_+(x)$ and $V_-(x)$ are shown in the inset.

4.3.3 Effect of the Boundary Conditions

The importance of solving the PB equation inside and outside the nanopore simultaneously is illustrated in Figure 4.4, where the solutions of the joint model and the conventional model with a fixed surface charge [30,32] are compared. The conventional method solves the PB equation inside and outside the nanopore independently assuming a boundary condition of zero surface charge. As a result, the obtained electrostatic potential at the inner surface of the nanopore is much lower that the potential at the outer surface. The inconsistency in the conventional model is that it leads to different potentials on the inner surface and the outer surface of the confining plate, which is impossible for a conductor. Even if the plate is not a

conductor, for instance an SAM, the potential drop means there is induced charge on both the surfaces, contradicting with the boundary condition that assumes no surface charge. The surface charge density is significant when the plate thickness is in the nanometer size. The assumption of zero surface charge in the conventional model is a good approximation only when the plate is very thick or the potential difference is very small. In both cases, the induced surface charge will be negligible.

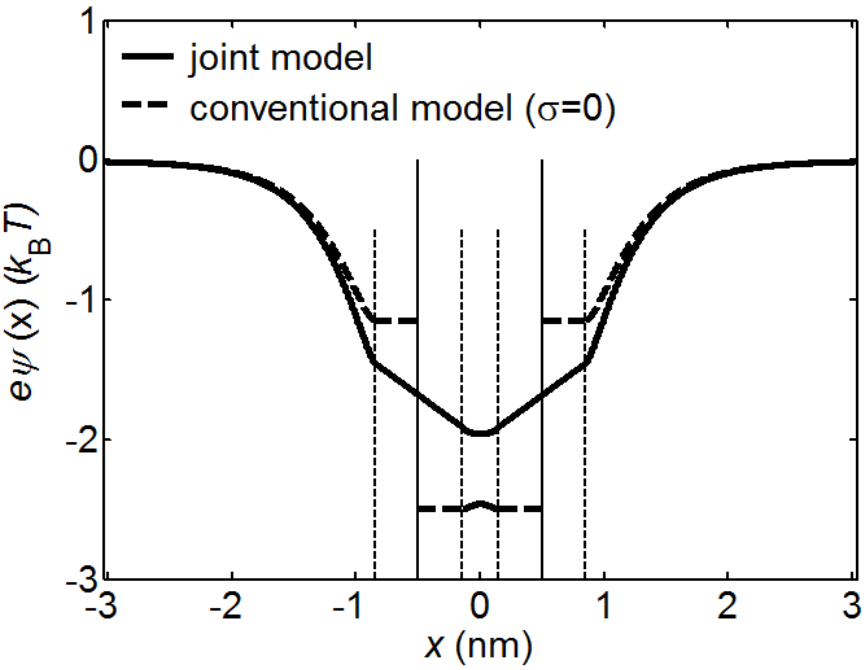

Figure 4.4: Comparing the PB equation solutions obtained using the joint model (solid line) and the conventional model that assumes a zero surface charge (dashed line). The solid vertical lines are the conducting plates and the dotted vertical lines are the Helmholtz planes.

The ion distributions from the two models are compared in Figure 4.5. Because the boundary condition of zero surface charge implies a neutrality of the total charge in the nanopore, the conventional model (dotted lines) predicts a much higher cation concentration and a much lower anion concentration than that of the joint model (solid lines).

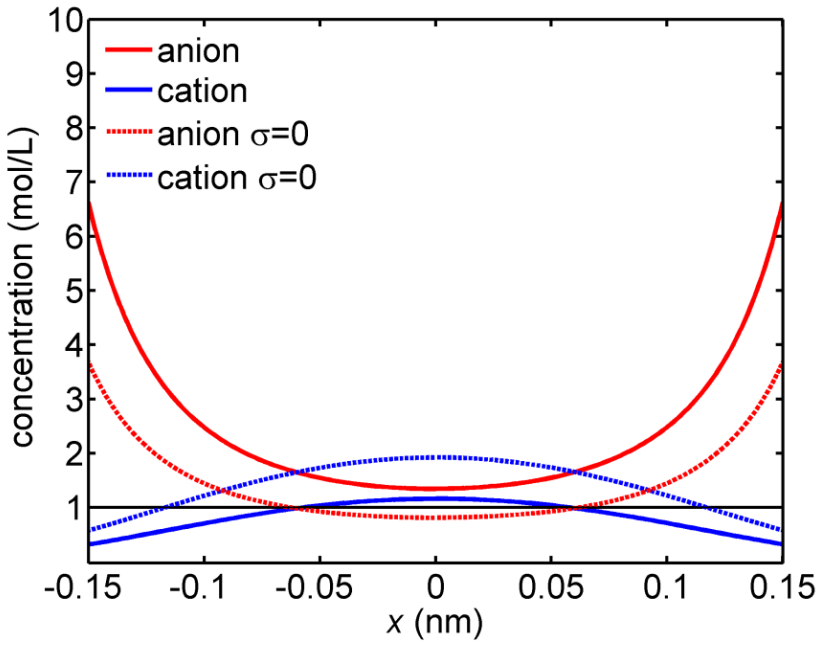

Figure 4.5: Comparing ion distributions inside the nanopore from the joint model (solid lines) and the conventional model (dotted line) that assumes a zero surface change.

4.3.4 Pore Size Dependence

It is not difficult to visualize the situation for very large pores where ions in the pore center do not feel the existence of the surface. Because there is no difference between the nanopore region and the bulk solution, the inner surface and outer surface of the conducting plate will be equivalent and both the surfaces has no induced surface charge. In this scenario, the two plates can be treated separately using the conventional boundary condition of zero surface charge density. As a result, the net charge in the EDL is zero on either side of the surface and the total charge in the nanopore is neutral. The counterintuitive electrolyte non-neutrality in the 1 nm pore suggests that the nanopore confinement plays an important role. The average ion concentration versus the pore size is shown in Figure 4.6. The B_i values are the same as in Figure 4.2. The electroneutrality breakdown is significant only when the pore size is less than 2 nm. As the pore

size increases, the concentration difference between cations and anions disappears and both ion concentrations approach the bulk value.

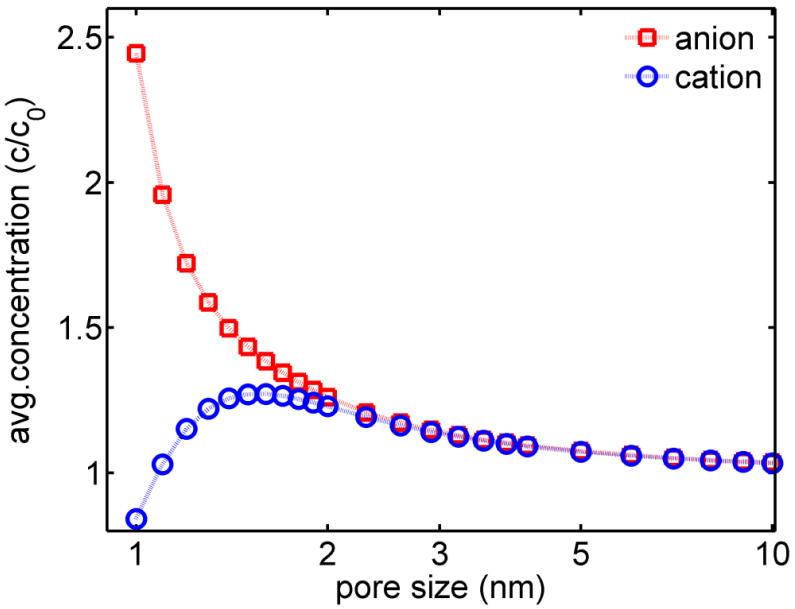

Figure 4.6: Average ion concentration in nanopores versus the pore size.

4.3.5 Specific Ion Effects on Electroneutrality Breakdown

Figure 4.7 shows the average ion concentration versus B_-, demonstrating the specific ion effects on the extent of the electroneutrality breakdown in 1 nm pores. Here, B_+ is fixed at 46×10^{-50} J m^3 while B_- varies from 40×10^{-50} J m^3 to -70×10^{-50} J m^3 to represent the increased ion affinity toward the interface. The average anion concentration increases as expected when B_- becomes more negative. Although B_+ is kept unchanged, the cation concentration also increases because of the increased electrostatic attraction to the anions. The electroneutrality breakdown is more significant as the difference between the cation's and the anion's affinity toward the surface grows. It is of note that the numerical calculation here shows a monotonic increase of the cation concentration. Such calculation could not explain the anomaly of the high Na^+

concentration in nanoconfined $NaNO_3$ electrolyte observed by the NMR measurements. This is mainly because the strong nonelectrostatic correlation between Na^+ and NO_3^-, which tend to bring more Na^+ into the nanopores, is not included in this calculation.

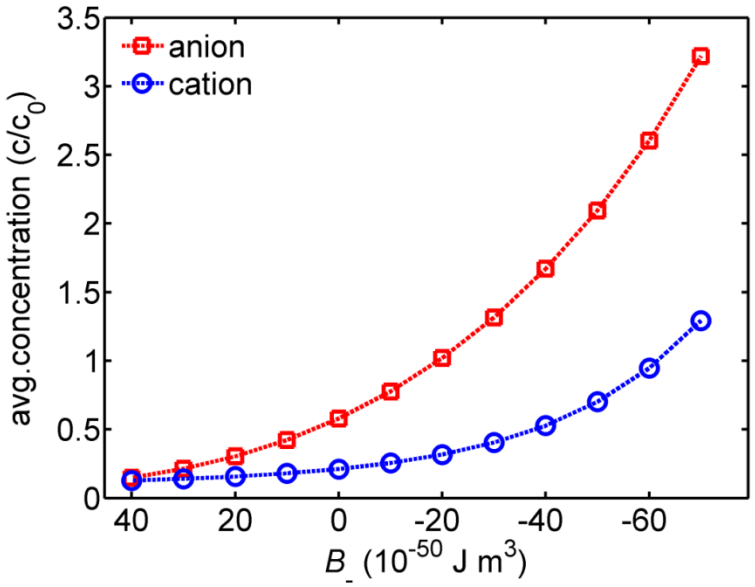

Figure 4.7: The average ion concentration in nanopores versus the parameter B_-. The parameter $B_+ = 46\times10^{-50}$ J m^3 is fixed.

4.4 Discussions

It is noted that the different ion size (hydrated or not) is also an important factor of the specific ion effects but the same ion radius in used in this calculation. This is due to the following two considerations: firstly, the essence of this calculation is to qualitatively estimate the role of the nonelectrostatic interactions. A simplified ion-surface potential due to any nonelectrostatic interaction is sufficient to illustrate this idea, regardless of its exact form and accuracy. Secondly, when a smaller cut-off distance is used for anions, the anion concentration inside the nanopore will be higher due to its stronger interaction with the surface. The cation concentration will increase as well because the cations will be attracted to the pores

electrostatically. Qualitatively, reducing the anion cut-off distance has a similar effect to that of increasing the anion-surface affinity (more negative B_{-}) and would not change the conclusion of the electroneutrality breakdown.

Another concern in the simulation is the assumption of the conducting plates. Activated carbon is far from a perfect conductor especially in the direction perpendicular to the basal plane. The specific capacitance on graphite basal plane is very small (only about 1~10 $\mu F/cm^2$) [38] and is mainly determined by the space charge capacitance [38-41]. Because of the relatively low density of states at the Fermi level, there is a considerable potential drop inside the solid [41]. However, the conducting plate assumption is not essential here and is mainly for the convenience of modeling. If a dielectric material with a nanometer thickness is used, the condition of an equal potential on both the inner and outer surfaces needs to be replaced with a more general potential continuity condition: a potential drop between the two surfaces that is consistent with the surface charge density and the dielectric constant of the electrode material. The electroneutrality breakdown would still be resulted although the extent might be smaller.

Prior works aiming at addressing the boundary conditions to solve the ion distribution inside nanopores are very rare, possibly because experimental approaches are lacking for such investigations. The MD simulations, although mostly enforcing the electroneutrality condition [42-45], have occasionally reported non-neutrality phenomena [46-48] for nanoconfined electrolyte in equilibrium with a reservoir. However their violation of electroneutrality is still qualitatively different from our observation. In their work, the non-neutrality occurs only when the surface is charged and the ionic charge in the nanopore does not balance the charge on the wall; the electroneutrality condition is not violated for an uncharged surface and the specific ion effects do not play a role.

To summarize, the generalized PB equation was successfully solved on a new model that does not require boundary conditions on surface charge. The ion distributions were solved both inside and outside the nanopore simultaneously with the condition of the potential continuity and net zero charge on the plates that provided the nanoconfinement. The ion-specific interfacial interactions including the ion-ion correlations were found to be responsible for the electroneutrality breakdown, in agreement with the NMR observations discussed in Chapter 3.

4.5 REFERENCES

1. Hansen, J.-P. and McDonald, I. R., *Theory of simple liquids: with applications to soft matter*. (Academic Press, 2013).

2. Israelachvili, J. N., *Intermolecular and surface forces: revised third edition*. (Academic press, 2011).

3. Levin, Y. *Rep. Prog. Phys.* **65**, 1577 (2002).

4. Borukhov, I., Andelman, D., *et al. Phys. Rev. Lett.* **79**, 435-438 (1997).

5. Boström, M., Williams, D. R. M., *et al. Phys. Rev. Lett.* **87**, 168103 (2001).

6. Horinek, D. and Netz, R. R. *Phys. Rev. Lett.* **99**, 226104 (2007).

7. Levin, Y., dos Santos, A. P., *et al. Phys. Rev. Lett.* **103**, 257802 (2009).

8. Bazant, M. Z., Storey, B. D., *et al. Phys. Rev. Lett.* **106**, 046102 (2011).

9. Skinner, B., Loth, M. S., *et al. Phys. Rev. Lett.* **104**, 128302 (2010).

10. Lauw, Y., Horne, M. D., *et al. Phys. Rev. Lett.* **103**, 117801 (2009).

11. Kalcher, I., Schulz, J. C., *et al. Phys. Rev. Lett.* **104**, 097802 (2010).

12. Levin, Y. *Phys. Rev. Lett.* **102**, 147803 (2009).

13. Messina, R., González-Tovar, E., *et al. EPL (Europhysics Letters)* **60**, 383 (2002).

14. Forsman, J. *J. Phys. Chem. B* **108**, 9236-9245 (2004).

15. Buyukdagli, S. and Ala-Nissila, T. *J. Chem. Phys.* **140**, 064701 (2014).

16. Kunz, W., *Specific ion effects*. (World Scientific, Singapore, 2010).

17. Murray, R. W. *Chem. Rev.* **108**, 2688-2720 (2008).

18. Arrigan, D. W. *Analyst* **129**, 1157-1165 (2004).

19. Conway, B., *Electrochemical supercapacitors: scientific fundamentals and technological applications*. (Kluwer Academic/Plenum. New York, 1999).

20. Huang, J., Sumpter, B. G., *et al. Angew. Chem. Int. Ed.* **47**, 520-524 (2008).

21. Winter, M. and Brodd, R. J. *Chem. Rev.* **104**, 4245-4270 (2004).

22. Kotz, R. and Carlen, M. *Electrochim. Acta* **45**, 2483-2498 (2000).

23. Chmiola, J., Yushin, G., *et al. Science* **313**, 1760-1763 (2006).

24. Zhu, Y., Murali, S., *et al. Science* **332**, 1537-1541 (2011).

25. Simon, P. and Gogotsi, Y. *Nature materials* **7**, 845-854 (2008).

26. Bocquet, L. and Charlaix, E. *Chem. Soc. Rev.* **39**, 1073-1095 (2010).

27. Schoch, R. B., Han, J., *et al. Rev. Mod. Phys.* **80**, 839 (2008).

28. Dekker, C. *Nat. Nanotechnol.* **2**, 209-215 (2007).

29. Luo, G., Malkova, S., *et al. Science* **311**, 216-218 (2006).

30. Kalcher, I., Schulz, J. C., *et al. J. Chem. Phys.* **133**, 164511 (2010).

31. Laanait, N., Mihaylov, M., *et al. Proc. Natl. Acad. Sci. U.S.A.* **109**, 20326-20331 (2012).

32. Lima, E., Horinek, D., *et al. J. Phys. Chem. B* **112**, 1580-1585 (2008).

33. Sata, T., *Ion exchange membranes: preparation, characterization, modification and application*. (Royal Society of Chemistry, 2004).

34. Hamann, C. H., Hamnett, A., *et al.*, *Electrochemistry*. (Wiley-VCH, 1998).

35. Rieger, P., *Electrochemistry*. (Chapman and Hall, New York, 1994).

36. Bonthuis, D. J., Gekle, S., *et al. Langmuir* **28**, 7679-7694 (2012).

37. Bonthuis, D. J., Gekle, S., *et al. Phys. Rev. Lett.* **107**, 166102 (2011).

38. Randin, J.-P. and Yeager, E. *Journal of Electroanalytical Chemistry and Interfacial Electrochemistry* **36**, 257-276 (1972).

39. Barbieri, O., Hahn, M., *et al. Carbon* **43**, 1303-1310 (2005).

40. Gerischer, H., McIntyre, R., *et al. J. Phys. Chem.* **91**, 1930-1935 (1987).

41. Gerischer, H. *The Journal of Physical Chemistry* **89**, 4249-4251 (1985).

42. Renou, R., Ghoufi, A., *et al. J. Phys. Chem. C* **117**, 11017-11027 (2013).

43. Argyris, D., Cole, D. R., *et al. ACS Nano* **4**, 2035-2042 (2010).

44. Kalluri, R. K., Konatham, D., *et al. J. Phys. Chem. C* **115**, 13786-13795 (2011).

45. Malani, A., Murad, S., *et al. Molecular Simulation* **36**, 579-589 (2010).

46. Lee, M. and Chan, K.-Y. *Chem. Phys. Lett.* **275**, 56-62 (1997).

47. Lo, W. Y. and Chan, K.-Y. *Mol. Phys.* **86**, 745-758 (1995).

48. Lozada-Cassou, M., Olivares, W., *et al. Physical Review E* **53**, 522 (1996).

CHAPTER 5 DEHYDRATION OF IONS IN VOLTAGE-GATED CARBON NANOPORES

The importance of the nonelectrostatic interfacial interactions in nanoconfined electrolytes has been demonstrated by both the NMR experiments in Chapter 3 and the numerical calculations in Chapter 4. In aqueous solutions, the interfacial interactions are always mediated by the solvent water and the properties of ion hydration play critical roles. Computational investigations in this subject are very active, but no experiments are currently available for monitoring *in-situ* the hydration status in the ionic processes inside nanopores in an electrochemical environment. In this chapter, the *in-situ* NMR is used to monitor the ion hydration status of electrolytes in charged nanopores, providing a molecular-scale understanding of the ionic processes in voltage-gated carbon nanopores.

5.1 Experimental Details and Results

5.1.1 NaF electrolytes in P-0 and P-92

The PEEK-derived activated carbon samples, P-0 and P-92, were used for this study. They have pore sizes 0.58 nm and 1.55 nm (wall surface to wall surface assuming slit-shaped pores) respectively [1]. The ^{1}H, ^{23}Na and ^{19}F static NMR spectra of 0.8 mol/kg NaF aqueous electrolytes in P-0 powders are shown in Figure 5.1. The peak centered at 0 ppm (chosen as reference) corresponds to water or ions in the intergranular spaces. The peak centered at -10.3 ppm of the ^{1}H spectrum corresponds to water inside the 0.58 nm pores. The upfield shift is due to the NICS effect [1,2] described above in Chapter 2. However, no such peaks are present in the ^{23}Na and ^{19}F spectra, indicating the absence of Na^{+} and F^{-} ions inside the nanopores because the

hydrated ion sizes (0.70 nm for F^- and 0.72 nm for Na^+) [3] are larger than the pore size. In contrast, the 1.55 nm pores in P-92 are accessible to the ions as demonstrated in Figure 5.2, where all the three spectra consist of three peaks. The chemical shift of nanoconfined water is around -4 ppm while that of the nanoconfined Na^+ and F^- is around -3.3 ppm. This is because the hydrated ions cannot approach the carbon surface as close as water molecules and, as a result, have a smaller NICS value.

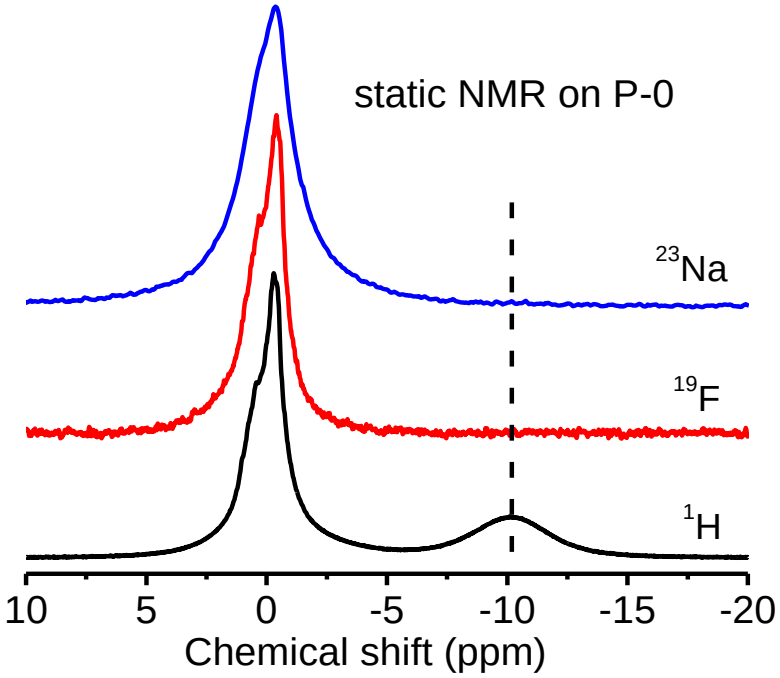

Figure 5.1: The static NMR spectra of NaF aqueous electrolyte in P-0 powders. Na^+ and F^- are excluded from the nanopores, so there is only one peak on the ^{23}Na and ^{19}F spectra. There are two peaks on the ^{1}H spectrum. The water in P-0 nanopores has a NICS value about -10 ppm.

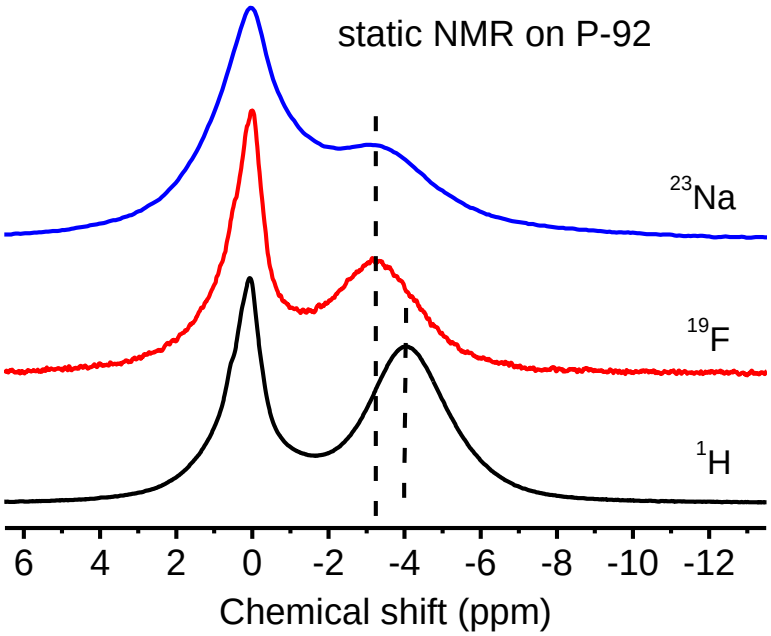

Figure 5.2: The static NMR spectra of NaF aqueous electrolyte in the P-92 sample. The 1.55 nm pores are accessible to the ions so each spectrum has two peaks. The chemical shift for the nanoconfined Na^+ and F^- (-3.3 ppm) differs slightly from that for water (-4 ppm) because the hydrated ions cannot approach the surface as closely as water.

5.1.2 F^- Permeation and Dehydration in P-0 Supercapacitor

The *in-situ* NMR measurements were carried out using the same setup described in Figure 3.2 in Chapter 3. The supercapacitor consists of two pure carbon electrodes separated by glass fibers. Both the carbon electrodes and the separator are immersed in a 0.8 mol/kg NaF aqueous electrolyte. The supercapacitor design is optimized for the NMR investigation of ion permeation rather than optimizing the charging rate as a normal supercapacitor does. Shielding one electrode with a copper foil enables the single-electrode study.

The F^- (Na^+) was investigated on the positive (negative) electrode via the ^{19}F (^{23}Na) NMR when the supercapacitor was charged from 0 V to 1.0 V with a 0.1 V step and thereafter discharged from 1.0 V to 0 V. Figure 5.3 shows the ^{19}F spectra from the positive electrode of the P-0 supercapacitor during the charging process. The signal intensity and the chemical shift of F^-

in nanopores are summarized Figure 5.4. Three stages are clearly identified: from 0 V to 0.3 V (stage I), the F^- ions are excluded from the nanopores; for an intermediate voltage (from 0.4 V to 0.7 V, stage II), F^- is attracted into the nanopores and the chemical shift stays around -9 ppm; under high voltage charging (from 0.8 V to 1.0 V, stage III), a dramatic change in chemical shift is observed while the ion intensity keeps on increasing.

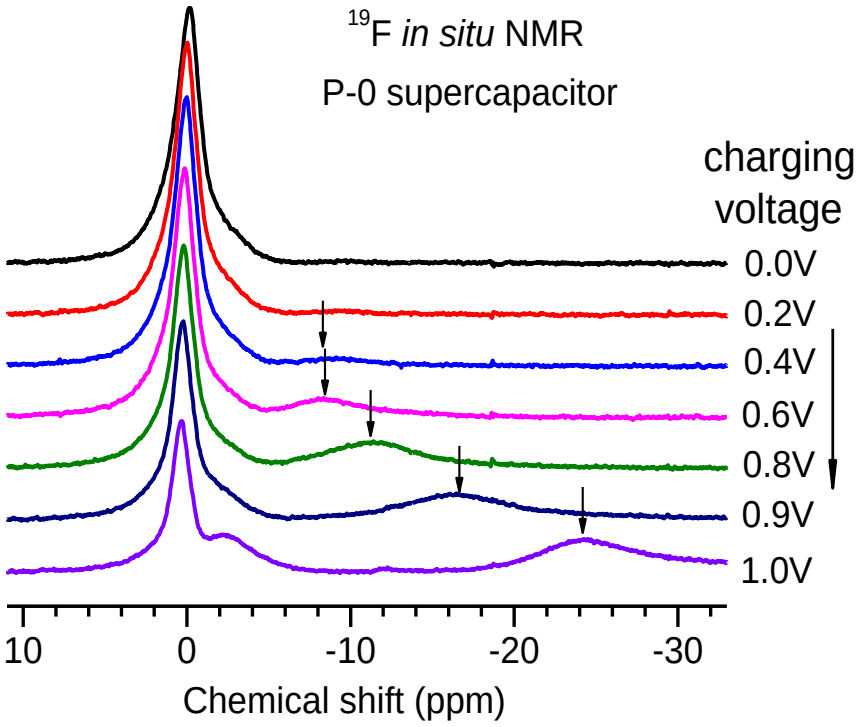

Figure 5.3: The ^{19}F spectra from the positive electrode of the P-0 supercapacitor. The peak around 0 ppm represents F^- in the separator and intergranular spaces. The peak corresponding to the intergranular ions moves slightly to the left (downfield, about 0.5 ppm at 1 V) due to the change in the bulk susceptibility.

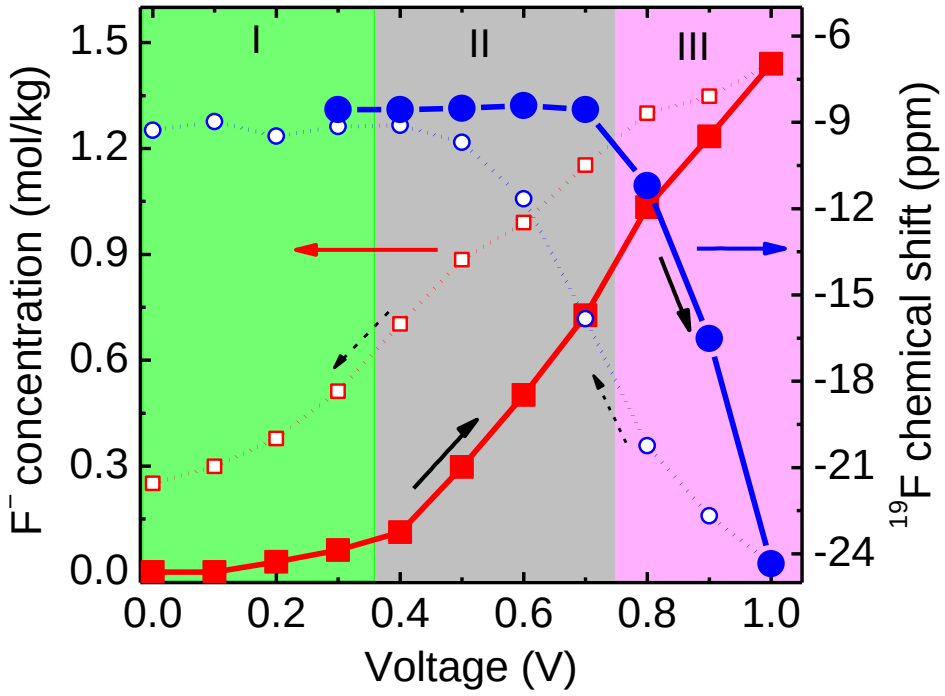

Figure 5.4: The ^{19}F chemical shift and intensity during positive charging. Three stages of the ion permeation are identified based on the chemical shift (blue marker) and the intensity (red marker) of F^- in the nanopores. The direction of the voltage change is indicated by the black arrow next to the curve.

Valuable insights into the permeation energetics and the hydration status can be gained by analyzing the NMR results where the ion permeation is monitored by the signal intensity and the hydration status is detected by the chemical shift. Computer simulations [4-8] show that F^- is a strongly hydrated ion with a hydration free energy of -119.7 kcal/mol, hydration number of 6 or 7 in the first shell, and no affinity toward a hydrophobic surface. Although a bare F^- is only 0.26 nm, the hydrated F^- is much larger in size (0.70 nm) and imposes an enormous energy barrier to the ion permeation into nanopores less than 2 nm as shown by the MD simulation [6]. This explains why the F^- ions are excluded from the P-0 nanopores (stage I in Figure 5.4). The permeation barrier is overcome by the electrostatic attractions in stage II so that a steady increase in intensity is observed. Surprisingly, the chemical shift of F^- in the nanopores (about -9 ppm) is similar to the NICS value of water in the P-0 nanopores, suggesting an intact first hydration shell

of F^-. Otherwise, a large change in chemical shift would appear because fewer water molecules in the first hydration shell would cause an upfield shift [5]. Of course the hydration shell must be reorganized or distorted in order to accommodate the 0.70 nm hydrated ions into the 0.58 nm pores. However, such distortion is not significant enough to affect the chemical shift at the charging voltage below 0.7 V. The 15 ppm upfield shift during stage III is a clear indication of the partial dehydration. The DFT calculation [5] shows an 13 ppm (26.9 ppm) upfield shift upon losing two (three) water molecule from the first hydration shell, suggesting an average loss of about two water molecules at 1.0 V charging in this experiment. The partial dehydration is reversible, although with some hysteresis, when the gating voltage is reduced from 1 V to 0 V. As illustrated in Figure 5.4 (open circles), the ^{19}F chemical shift is fully recovered to -9 ppm, but at a smaller voltage (0.5 V) than the partial dehydration onset voltage (0.7 V). The F^- intensity doesn't return to zero at 0V, indicating that some anions are trapped in the nanopores.

5.1.3 Na^+ in P-0 Supercapacitor

The Na^+ permeation on the negative electrode is found to differ from F^- in three aspects. Firstly, the barrier for Na^+ to enter the 0.58 nm pore in P-0 is larger than the barrier for F^- as evidenced by the higher taking-off voltage (0.6 V for Na^+ vs. 0.4 V for F^-). This is opposite to the predictions in the MD simulations [6,9]. The failure in the MD prediction might be due to the lack of polarizability in the calculations, a factor that is critical in the interfacial interactions [8,10-13]. Secondly, the Na^+ intensity is considerably smaller than that of F^- at the same charging voltage, in agreement with the higher barrier for Na^+. Thirdly, in contrast to F^-, no significant change in chemical shift is observed for Na^+ on the negative electrode even at 1 V charging.

A DFT calculation was carried out to estimate the dependence of ^{23}Na chemical shift on the hydration number. A fully hydrated Na^+ has four water molecules in the first shell. $Na^+(H_2O)_n$ clusters with n=1 to 4 are optimized using Gaussian [14] at the B3LYP/6-311+g(d) level for the structures adopted from previous studies [15,16]. The NMR chemical shift is then calculated using the GIAO method [17]. The results are listed in Table 5.1, which shows that ^{23}Na chemical shift is also sensitive to the hydration number in the first shell. The constant ^{23}Na chemical shift in the experiment indicates that a partial dehydration is not induced even at 1 V charging.

Table 5.1: The ^{23}Na chemical shift of $Na^+(H_2O)_n$ cluster (n=1,2, 3,4).

Hydration number	0	1	2	3	4
Chemical shift (ppm, arbitrary reference)	623.6	601.2	580.7	567.9	560.8

5.1.4 *In-situ* Charging on P-92 supercapacitor

The voltage-induced partial dehydration process in the voltage-gated nanopores was further demonstrated by the *in-situ* NMR experiments on a P-92 supercapacitor where the larger pore size (1.55 nm) is accessible to both F^- and Na^+ without charging. The ^{19}F chemical shift moves downfield between 0 V and 0.7 V then turns upfield, as demonstrated in Figure 5.5. The downfield shift is caused by the field effect that changes the Fermi level upon charging. Previous studies on graphene [18,19] and graphite basal planes [20-22] have shown the change of the Fermi level induced by a voltage gating (both positive and negative charging). Therefore the downfield shift of the NICS value during charging is expected.

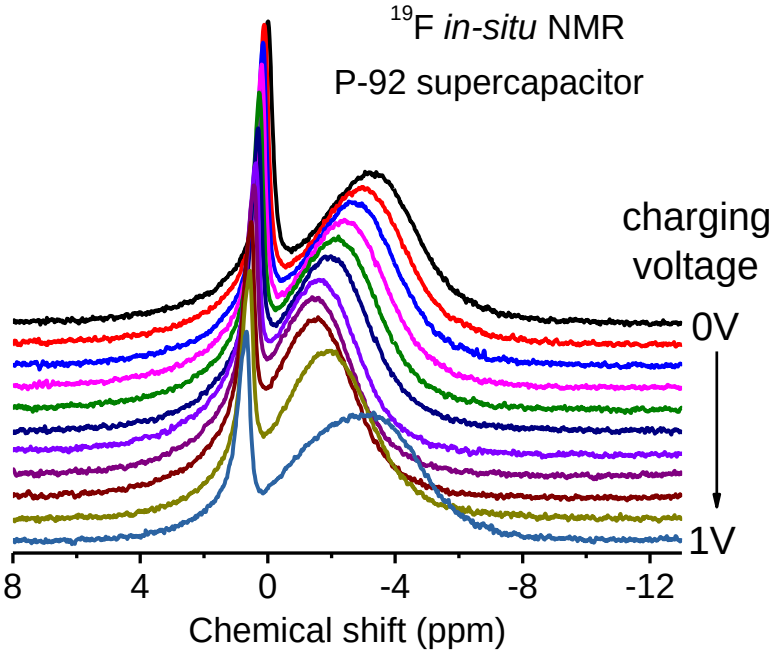

Figure 5.5: The ^{19}F spectra evolution on the positive electrode as the charging voltage increases.

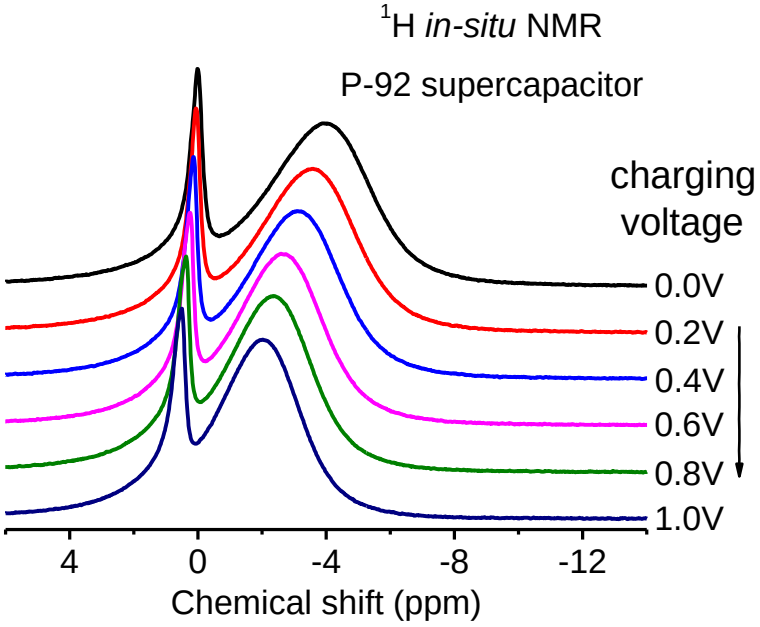

Figure 5.6: The ^{1}H spectra evolution on the positive electrode as the charging voltage increases. The center of the right peak changes linearly with voltage.

The ^{1}H NMR on nanoconfined water was carried out at the same time to monitor the gating-voltage dependent NICS values [2,23], which shows a linear dependence of the chemical

shift on the charging voltage (Figure 5.6). Since this change is caused by the carbon material and therefore is identical to all species, including F^-, inside the nanopores, subtracting this from the ^{19}F chemical shift gives rise to the contribution due to the ion dehydration. The adjusted ^{19}F chemical shift exhibits a flat region up to 0.7 V then starts moving upfield, which is a clear indication of the voltage-induced partial dehydration. It is interesting to note that the upfield shift (-2 ppm between 0.7 V and 1.0 V) is considerably smaller than that in the P-0 supercapacitor. The P-92 sample has a much larger pore size, so more fully hydrated ions can reside in the pore space. The dynamic exchange between the fully hydrated ions away from the walls and the partially dehydrated ions adsorbed on the nanopore walls leads to a much smaller change in the chemical shift. It is also intriguing that the dehydration process in the 1.55 nm pores has the same onset voltage as in the 0.58 nm pores, suggesting that the dehydration is caused primarily by the voltage gating instead of the nanopore confinement.

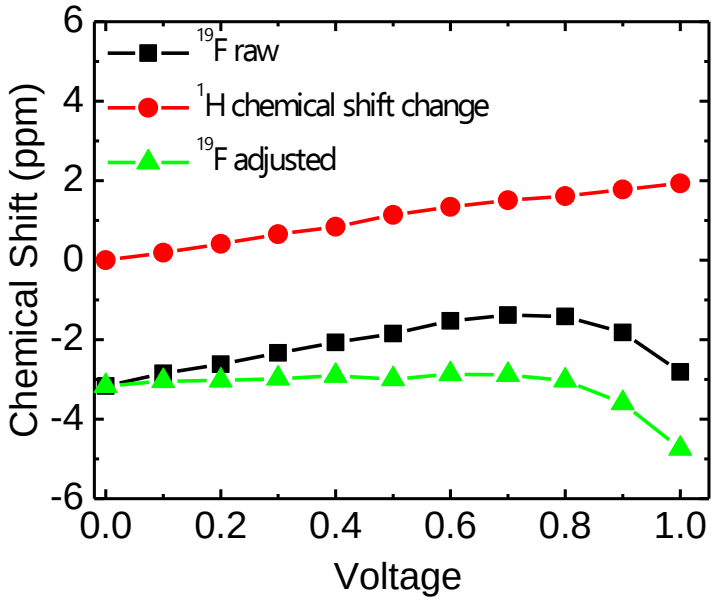

Figure 5.7: The ^{19}F and ^{1}H chemical shift versus the charging voltage. The green line, which shows the contribution from the dehydration, is obtained by subtracting the red line from the red line.

5.2 Discussions

The destruction of the hydration shell at the electrochemical interface has been discussed for a long time since the inception of the EDL theory and recently it was experimentally demonstrated by Yamakata et al. [24,25]. The *in-situ* NMR results here show a similar voltage-induced dehydration process inside the nanopore confinement, whereas the ion permeation is greatly affected by the pore size. These observations can provide insights in the energy storage mechanism in carbon supercapacitors. It is generally believed that the ion desolvation is responsible for the anomalous capacitance increase in the sub-nanometer pores [26-28]. This study shows that this is not the case. The voltage-induced ion dehydration occurs in both the small pores in P-0 and large pores in P-92, therefore the dehydration process itself could not explain the anomalous capacitance increase. Instead, the barrier on the ion permeation into the nanopores might be the key to unveil the mechanism because it directly influence the charge stored in the carbon nanopores. Such a barrier is not necessary due to the desolvation.

In summary, this chapter demonstrated a direct experimental observation of the ion permeation and dehydration in voltage-gated carbon nanopores. The NICS effect on activated carbon systems allows a selective study of the ionic processes inside nanopores. The *in-situ* NMR experiment reveals the partial dehydration of F^- in the carbon nanopores and a higher energetic barrier for Na^+ than for F^-. The NICS-based *in-situ* NMR approach could have profound implications in research areas such as nanofluidics, water desalination and energy storage devices, providing valuable insights into the ion permeation in nanochannels.

5.3 REFERENCES

1. Xing, Y.-Z., Luo, Z.-X., *et al. Carbon* **77**, 1132-1139 (2014).
2. Forse, A. C., Griffin, J. M., *et al. J. Phys. Chem. C* **118**, 7508–7514 (2014).
3. Israelachvili, J. N., *Intermolecular and surface forces: revised third edition*. (Academic press, 2011).
4. Zhan, C.-G. and Dixon, D. A. *The Journal of Physical Chemistry A* **108**, 2020-2029 (2004).
5. Gerken, M., Boatz, J. A., *et al.*, in *J. Fluorine Chem.* (2002), Vol. 116, pp. 49-58.
6. Richards, L. A., Schäfer, A. I., *et al. Small* **8**, 1701-1709 (2012).
7. Jungwirth, P. and Tobias, D. J. *J. Phys. Chem. B* **105**, 10468-10472 (2001).
8. Jungwirth, P. and Tobias, D. J. *Chem. Rev.* **106**, 1259-1281 (2006).
9. Beckstein, O., Tai, K., *et al. J. Am. Chem. Soc.* **126**, 14694-14695 (2004).
10. Chen, X., Yang, T., *et al. J. Am. Chem. Soc.* **129**, 12272-12279 (2007).
11. Zhang, Y. and Cremer, P. S. *Proc. Natl. Acad. Sci. U.S.A.* **106**, 15249-15253 (2009).
12. Lauw, Y., Horne, M. D., *et al. Phys. Rev. Lett.* **103**, 117801 (2009).
13. Kunz, W., *Specific ion effects*. (World Scientific, Singapore, 2010).
14. Frisch, M., Trucks, G., *et al. Gaussian Inc., Wallingford CT* (2010).
15. Hashimoto, K. and Morokuma, K. *J. Am. Chem. Soc.* **116**, 11436-11443 (1994).
16. Barnett, R. and Landman, U. *Phys. Rev. Lett.* **70**, 1775 (1993).
17. Wolinski, K., Hinton, J. F., *et al. J. Am. Chem. Soc.* **112**, 8251-8260 (1990).
18. DasA, PisanaS, *et al. Nat Nano* **3**, 210-215 (2008).
19. Xia, J., Chen, F., *et al. Nat Nano* **4**, 505-509 (2009).
20. Gerischer, H. *The Journal of Physical Chemistry* **89**, 4249-4251 (1985).
21. Randin, J.-P. and Yeager, E. *Journal of Electroanalytical Chemistry and Interfacial Electrochemistry* **36**, 257-276 (1972).
22. Gerischer, H., McIntyre, R., *et al. J. Phys. Chem.* **91**, 1930-1935 (1987).

23. Deschamps, M., Gilbert, E., *et al. Nature materials* (2013).

24. Yamakata, A., Soeta, E., *et al. J. Am. Chem. Soc.* **135**, 15033-15039 (2013).

25. Yamakata, A. and Osawa, M. *J. Am. Chem. Soc.* **131**, 6892-6893 (2009).

26. Chmiola, J., Largeot, C., *et al. Angew. Chem.* **120**, 3440-3443 (2008).

27. Chmiola, J., Yushin, G., *et al. Science* **313**, 1760-1763 (2006).

28. Huang, J., Sumpter, B. G., *et al. Angew. Chem. Int. Ed.* **47**, 520-524 (2008).

CHAPTER 6 CONCLUSIONS

This dissertation discussed several studies on water and aqueous electrolytes confined in activated carbon nanopores. Because of the unique electronic structure of the graphitic surface, molecules residing inside the carbon nanopores give rise to a different NMR chemical shift from those outside. This NICS mechanism was employed to characterize the PSD of activated carbons with the aid of DFT calculations which established a quantitative relationship between the pore size and the NICS value. Compared to other techniques for PSD measurements, the NMR method is fast, convenient and very sensitive in the micropore region. Only one ^{1}H MAS spectrum for water adsorbed in the activated carbons is required to derive the PSD from the NMR spectrum lineshape.

Understanding the physics of electrolytes in activated carbon nanopores is critical for revealing the charge storage mechanism in carbon supercapacitors and to explain the anomalous capacitance increase inside carbon nanopores less than 1 nm. The ^{1}H, ^{23}Na, ^{19}F and ^{15}N NMR were carried out to quantify the ion concentrations inside carbon nanopores and demonstrated a substantial electroneutrality breakdown for nanoconfined aqueous electrolytes in equilibrium with a bulk reservoir. A series of sodium salts, where the anions were chosen from the Hofmeister series, were systematically studied. Different anion concentrations were observed although the electrolyte concentration and the carbon pore size were the same. The sodium cation concentrations are greatly influenced by the anions. This suggests that the interfacial specific ion effects and the ion-ion correlations play crucial roles in determining the degree of the electroneutrality breakdown. The *in-situ* NMR was carried out on a carbon supercapacitor

built into the NMR probe. The dependence of the ion concentration on the charging voltage exhibited different behaviors for cations and anions. Interestingly, the sodium cation concentration on the negative electrode first increases then decreases for the $NaBF_4$ electrolyte and remains nearly independent of the charging voltage for the $NaNO_3$ electrolytes. Those observations demonstrated the significant influence of the nonelectrostatic interactions on the behavior of electrolytes in nanoconfinement.

A numerical calculation of the ion distribution in nanopores was implemented using the generalized PB equation on a new nanopore model. The generalized PB equation takes into account both the electrostatic and nonelectrostatic interactions. The boundary conditions on the surface charge density are not required in the new model and therefore permit an induced surface charge. The ion distributions were solved both inside and outside the nanopore simultaneously. The results confirmed the electroneutrality breakdown inside the nanopores. As the difference in the ion-surface interfacial interactions between cations and anions increases, the electrolyte non-neutrality becomes more profound. The ion affinity toward the interface controls whether ions are depleted or accumulate inside the nanopores. The electroneutrality breakdown also depends sensitively on the pore size and disappears in pores larger than 2 nm, indicating that it is indeed dominated by the short-ranged interfacial interactions.

In aqueous electrolytes, the interfacial interactions are always mediated by the solvent water. The ion hydration is an essential part of the specific ion effects. With the *in-situ* ^{23}Na and ^{19}F NMR on carbon supercapacitors with different carbon pore sizes, a molecular scale understanding was provided for the permeation and dehydration of ions in voltage-gated carbon nanopores. The NMR intensity and chemical shift provide information on the ion permeation and hydration status, respectively. For nanopores larger than the bare F^- ion size but slightly smaller

than the hydrated ion size, F^- cannot enter the nanopores at a charging voltage of less than 0.4 V. The ion permeation into the nanopores starts after 0.4 V with its first hydration shell preserved. The partial dehydration occurs above the gating voltage of 0.7 V, as indicated by the huge upfield chemical shift. In contrast, the dehydration process does not occur for Na^+ ions even at 1.0 V charging because of the stronger Na^+ hydration. For the larger pore size in P-92 which is accessible to ions even without charging, a similar dehydration process is induced by a gating voltage above 0.7 V.